Draft version November 21, 2016
Preprint typeset using LaTeX style emulateapj v. 5/2/11

arXiv:1611.06027v1 [astro-ph.GA] 18 Nov 2016

CHEMICAL EVOLUTION OF THE UNIVERSE AT $0.7 < Z < 1.6$ DERIVED FROM ABUNDANCE DIAGNOSTICS OF THE BROAD-LINE REGION OF QUASARS

H. Sameshima[1], Y. Yoshii[2] and K. Kawara[2,3]

Draft version November 21, 2016

ABSTRACT

We present an analysis of Mg II λ2798 and Fe II UV emission lines for archival Sloan Digital Sky Survey (SDSS) quasars to explore diagnostics of the magnesium-to-iron abundance ratio in a broad-line region cloud. Our sample consists of 17,432 quasars selected from the SDSS Data Release 7 with a redshift range of $0.72 < z < 1.63$. A strong anticorrelation between Mg II equivalent width (EW) and the Eddington ratio is found, while only a weak positive correlation is found between Fe II EW and the Eddington ratio. To investigate the origin of these differing behaviors of Mg II and Fe II emission lines, we have performed photoionization calculations using the Cloudy code, where constraints from recent reverberation mapping studies are considered. We find from calculations that (i) Mg II and Fe II emission lines are created at different regions in a photoionized cloud, and (ii) their EW correlations with the Eddington ratio can be explained by just changing the cloud gas density. These results indicate that the Mg II/Fe II flux ratio, which has been used as a first-order proxy for the Mg/Fe abundance ratio in chemical evolution studies with quasar emission lines, depends largely on the cloud gas density. By correcting this density dependence, we propose new diagnostics of the Mg/Fe abundance ratio for a broad line region cloud. Comparing the derived Mg/Fe abundance ratios with chemical evolution models, we suggest that α-enrichment by mass loss from metal-poor intermediate-mass stars occurred at $z \sim 2$ or earlier.

Subject headings: galaxies: active — quasars: emission lines — galaxies: abundances

1. INTRODUCTION

Investigating heavy-element abundances of distant objects over a range of redshift is essential for understanding the history of star formation in the Universe. In particular, the abundance ratio of α-elements such as O, Ne, Mg, and so on relative to Fe has drawn intense research interest. As is commonly known from nucleosynthesis calculations, type II supernovae (SNe II) from massive stars mainly supply α-elements, while type Ia supernovae (SNe Ia) from binary systems mainly supply iron (e.g., Nomoto et al. 1997a,b). Since the lifetime of SN Ia is estimated to be typically $t_{\rm Ia} \sim 1$ Gyr[4] (Greggio & Renzini 1983; Matteucci & Greggio 1986) which is 1–2 orders longer than that of SN II, the iron enrichment should be delayed behind α, causing a break in $[\alpha/{\rm Fe}]$[5] at the elapsed time $t \sim t_{\rm Ia}$ from the formation of the first stars (e.g., Hamann & Ferland 1993, 1999; Yoshii et al. 1996, 1998). Such a break, although confirmed from observations of long-lived metal-poor stars in the solar neighborhood, still requires confirmation at high redshift corresponding to $t \sim t_{\rm Ia}$ in the early Universe.

In this context, quasars offer a valuable tool for exploring the $[\alpha/{\rm Fe}]$ break at high redshift, because (i) their spectra show plenty of emission and absorption lines of metals including α elements and iron, and (ii) their brightness is great enough to provide spectra of good quality even from a far distance at $z > 7$ (e.g., Mortlock et al. 2011). Measuring the emission-line flux ratio is one method that can be used to derive the abundance ratio, and the emission lines from Mg II and Fe II have been considered as an ideal line pair. Their similar ionization energies would cause these two ions to coexist at a similar location in a broad-line region (BLR) cloud. This assumption is partly supported by recent reverberation mapping studies, which imply that the Fe II emission region in quasars exists at a similar location to Hβ that represents other broad emission lines including Mg II (e.g., Chelouche et al. 2014, Shen et al. 2016).[6] Therefore, the flux ratio would be at least linearly related to the abundance ratio (e.g., Hamann & Ferland 1999).

Fe II emission lines observed in quasar spectra were thus eagerly studied in the 1970s and 1980s (e.g., Osterbrock 1977; Phillips 1978a,b; Collin-Souffrin et al. 1979, 1980; Kwan & Krolik 1981; Joly 1981; Grandi 1981). From their photoionization calculations and comparison with observations, Netzer & Wills (1983) and Wills et al. (1985) showed that iron is presumably overabundant in comparison with the solar value for quasars, having large Fe II flux relative to Mg II. Under these circumstances, the Mg II/Fe II flux ratio was assumed to be a first-order proxy for the Mg/Fe abundance ratio, and has been measured over a wide range of redshift extending to $z \sim$

[1] Laboratory of Infrared High-resolution spectroscopy (LIH), Koyama Astronomical Observatory, Kyoto Sangyo University, Motoyama, Kamigamo, Kita-ku, Kyoto 603-8555, Japan. E-mail: sameshima@cc.kyoto-su.ac.jp
[2] Institute of Astronomy, School of Science, University of Tokyo, 2-21-1 Osawa, Mitaka, Tokyo 181-0015, Japan
[3] Deceased January 2015.

[4] Recent studies, however, show that the $t_{\rm Ia}$ distribution is more weighted toward a shorter life time for SNe Ia (e.g., Totani et al. 2008; Maoz et al. 2012).

[5] $[\alpha/{\rm Fe}] \equiv \log(n_\alpha/n_{\rm Fe}) - \log(n_\alpha/n_{\rm Fe})_\odot$, where n_x represents the number density of the element $x(=\alpha$ or Fe).

[6] These reverberation studies, however, do not exclude the possibility that the Fe II emission region could be twice as large as that of Hβ, so the locations of the Fe II and Mg II regions may not be the same (Barth et al. 2013; Chelouche et al. 2014).

7 (e.g., Kawara et al. 1996; Thompson et al. 1999; Freudling et al. 2003; Barth et al. 2003; Maiolino et al. 2003; Dietrich et al. 2002, 2003; Iwamuro et al. 2002, 2004; Tsuzuki et al. 2006; Jiang et al. 2007; Kurk et al. 2007; Sameshima et al. 2009; De Rosa et al. 2011, 2014; and references therein). However, the measured flux ratios show a large scatter beyond measurement errors, especially at high redshift, preventing us from finding any signature for the [Mg/Fe] break.

Doubt is then cast on the usual assumption that the Mg II/Fe II flux ratio is a first-order proxy for the Mg/Fe abundance ratio (De Rosa et al. 2011). Baldwin et al. (2004) systematically investigated Fe II emission lines by using the photoionization CLOUDY code combined with the 371-level Fe^+ model (Verner et al. 1999). Their calculations show that the strength of the Fe II emission lines depends not only on iron abundance, but also on gas density, the ionization parameter, column density, and microturbulence. Verner et al. (2003) also argued the importance of such dependence using their original 830-level Fe^+ model. Therefore, the large scatter observed for Mg II/Fe II may be accounted for by the effects of non-abundance parameters that may differ from quasar to quasar.

In fact, Dong et al. (2011) found that Mg II/Fe II strongly correlates with the Eddington ratio. They also argued that in most plausible scenarios connecting active galactic nuclei (AGNs) and starburst activities (e.g., Davies et al. 2007), the delay between the two events is less than 1 Gyr, so α-elements should be enhanced relative to iron during the active phase of AGNs. An anticorrelation between Mg II/Fe II and the Eddington ratio is then naturally expected, whereas the observation contradicts it. These results imply the existence of non-abundance parameters that would seriously affect Mg II/Fe II. In summary, there is growing evidence that the Mg II/Fe II flux ratio is only a "second-order" proxy for the Mg/Fe abundance ratio. However, there have been few reports as to whether the abundance information can be extracted quantitatively from observables against these non-abundance effects.

The purpose of this paper is to invent reliable diagnostics of the Mg/Fe abundance ratio for a BLR cloud. A sufficient number of quasars selected from the Sloan Digital Sky Survey (SDSS; York et al. 2000) are analyzed to measure their Mg II/Fe II flux ratios, and photoionization calculations are carried out to interpret Mg II/Fe II in terms of the Mg/Fe abundance ratio. This paper is organized as follows. In Section 2, we describe the sample selection and the data reduction of SDSS quasars. In Section 3, measured emission-line strengths of the SDSS quasars are summarized. In Section 4, parameter setting for the photoionization model is described, and the results are given in Section 5. In Section 6, we discuss the dependence of Mg II/Fe II on non-abundance parameters, propose new abundance diagnostics for a BLR cloud, and compare the derived Mg/Fe abundance ratios with chemical evolution models to constrain star formation history. In Section 7, a summary and conclusion are given. Throughout this paper, we assume ΛCDM cosmology, with $\Omega_\Lambda = 0.7$, $\Omega_M = 0.3$, and $H_0 = 70$ km s^{-1} Mpc^{-1}.

2. SDSS DATA ANALYSIS

Our sample is selected from the quasar catalog of the SDSS Data Release 7 (DR7), in which 105,783 spectroscopically confirmed quasars are included (Schneider et al. 2010). The following two criteria are adopted for our sample selection. Firstly, a rest frame wavelength range of 2200–3500Å is available; this is required to measure both Fe II and Mg II emission lines, and the continuum level around them. Since the wavelength range covered by the spectroscopic observation in the SDSS DR7 is 3800–9200Å, this criterion confines the redshift range within $0.72 < z < 1.63$. Secondly, the median value of the signal to noise ratios (S/Ns) in the entire wavelength range of the SDSS spectra is larger than 10 pix^{-1}; from experience, this is required for accurate measurement of Fe II and Mg II emission lines. We find that 17,468 objects fulfill these two criteria. According to the catalog given by Shen et al. (2011), 254 objects out of 17,468 are flagged as broad absorption line (BAL) quasars. Although these BAL quasars are not excluded in the following analysis, we note that whether or not these are excluded from our sample affects none of the conclusions of this paper.

The fluxes of the Mg II and Fe II emission lines are measured for the selected quasars in almost the same way as that used by De Rosa et al. (2011). Firstly, the following continuum model is fitted to each spectrum:

$$F_\lambda = F_\lambda^{\rm PL}(\alpha, \beta) + F_\lambda^{\rm BaC} + F_\lambda^{\rm FeII}(\gamma), \quad (1)$$

where $F_\lambda^{\rm PL}$ is a power-law continuum flux emitted from an accretion disk, $F_\lambda^{\rm BaC}$ is a Balmer continuum flux and $F_\lambda^{\rm FeII}$ is a Fe II pseudo-continuum flux. Following De Rosa et al. (2011), we adopt the Balmer continuum model given by Grandi (1982) for $F_\lambda^{\rm BaC}$; the shape and the flux ratio against the power-law component are fixed to those adopted by De Rosa et al. (2011). Unlike De Rosa et al. (2011), however, we use the Fe II template given by Tsuzuki et al. (2006) instead of that of Vestergaard & Wilkes (2001); this is because the latter does not cover the wavelength range around the Mg II emission line. Prior to fitting, the Fe II template is broadened by convolution with a Gaussian function for which the full width at half maximum (FWHM) is fixed[7] at 2,000 km s^{-1}. There are thus three free parameters: the power-law slope (α), the normalization of the power-law continuum flux (β), and the normalization of the Fe II pseudo-continuum flux (γ). The best fit parameters are obtained by performing χ^2 minimization with the IDL procedure `MPFIT.pro` (Markwardt 2009). Fe II flux is calculated by integrating the fitted Fe II template in a wavelength range of 2200–3090Å. Then, fitting of the Mg II λ2798 emission line is performed; two Gaussians are fitted to the continuum-subtracted spectrum at the rest frame wavelength range of 2700–2900Å with the `MPFIT.pro` procedure. Both the flux and the FWHM of Mg II are calculated from the sum of the two fitted Gaussians. In these processes, there are failures in the fittings for 36 quasars. However, since the number is too small to affect the result, we have decided to exclude them from the following analysis.

[7] Note that, as De Rosa et al. (2011) pointed out, the measured Fe II flux depends very little on the FWHM adopted for the convolved Gaussian function.

The mass of a black hole (BH), or $M_{\rm BH}$, is estimated from the Mg II FWHM and the continuum luminosity at 3000Å by using the virial mass estimate formula (Vestergaard & Osmer 2009):

$$\log\left(\frac{M_{\rm BH}}{M_\odot}\right) = 6.86 + 2\log\left(\frac{\rm FWHM(MgII)}{1,000\ {\rm km\ s^{-1}}}\right) + 0.5\log\left(\frac{\lambda L_\lambda(3000{\rm \AA})}{10^{44}\ {\rm erg\ s^{-1}}}\right). \quad (2)$$

The Eddington luminosity is defined as the luminosity at which the radiation force acting on an electron–proton pair is balanced with the gravitation force exerted on the pair. For a BLR cloud orbiting the central BH, the Eddington luminosity is given by

$$L_{\rm Edd} = \frac{4\pi G c m_p}{\sigma_e} M_{\rm BH}, \quad (3)$$

where G is the gravitational constant, c is the speed of light, m_p is the proton mass, and σ_e is the Thomson scattering cross section (Peterson 1997). Following Shen et al. (2011), we estimate the bolometric luminosity from the measured monochromatic luminosity at 3000Å with the bolometric correction formula:

$$L_{\rm bol} = 5.15\lambda L_\lambda(3000{\rm \AA}). \quad (4)$$

From equations (2)–(4), the Eddington ratio is written as

$$\log\left(\frac{L_{\rm bol}}{L_{\rm Edd}}\right) = -0.249 - 2\log\left(\frac{\rm FWHM(MgII)}{1,000\ {\rm km\ s^{-1}}}\right) + 0.5\log\left(\frac{\lambda L_\lambda(3000{\rm \AA})}{10^{44}\ {\rm erg\ s^{-1}}}\right). \quad (5)$$

For all the quasars in our sample, the Eddington ratio is evaluated using this formula.

In summary, our final sample consists of 17,432 quasars in the redshift range of $0.72 < z < 1.63$. Figure 1 shows histograms of the measured values of various quantities such as redshift, monochromatic luminosity at 3000Å, rest-frame equivalent widths (EWs) of Fe II and Mg II, BH mass, and the Eddington ratio of our sample of SDSS quasars. The EWs of Fe II and Mg II emission lines are calculated by dividing the measured flux by the continuum flux density at 3000Å. As previous studies have pointed out (Marziani et al. 2003; Dong et al. 2011), `MPFIT.pro` likely underestimates measurement errors, because it does not account for potential systematic errors related to, e.g., Fe II pseudocontinuum subtraction. Therefore, typical measurement errors are estimated by Monte Carlo simulations (see Sameshima et al. 2011) as follows: 16% for EW(Fe II), 7.2% for EW(Mg II), 7.9% for FWHM(Mg II), and 10% for $\lambda L_\lambda(3000{\rm \AA})$. Figure 2 plots the measured Mg II/Fe II flux ratios against their redshifts. It is clear that Mg II/Fe II shows no significant evolution at $z \sim 1$–2. This result is consistent with Iwamuro et al. (2002), in whose analysis an earlier version of the SDSS data was used.

3. EW(FE II) VERSUS EW(MG II) DIAGRAM

From comparison of the measured values, we find that EW(Mg II) positively correlates with EW(Fe II), as seen from the log EW(Fe II) versus log EW(Mg II) plot in Figure 3. To examine how this correlation depends on the Eddington ratio, we divide our sample into five subsamples: (i) $L_{\rm bol}/L_{\rm Edd} < 10^{-1.0}$, (ii) $10^{-1.0}$–$10^{-0.75}$, (iii) $10^{-0.75}$–$10^{-0.5}$, (iv) $10^{-0.5}$–$10^{-0.25}$, and (v) $> 10^{-0.25}$. These sub-samples are shown by different colors in Figure 3. It is evident that quasars with larger $L_{\rm bol}/L_{\rm Edd}$ tend to have smaller EW(Mg II).

TABLE 1
Correlations with the Eddington ratio.

Quantity (y)	Slope (a)	Intercept (b)	$\rho^\dagger$
Mg II/Fe II	-0.368 ± 0.005	-0.779 ± 0.003	-0.73
EW Mg II (Å)	-0.298 ± 0.005	$+1.250 \pm 0.003$	-0.64
EW Fe II (Å)	$+0.068 \pm 0.007$	$+2.026 \pm 0.004$	$+0.08$

Note. — Linear regression analysis is performed with $\log y = a \times \log L_{\rm bol}/L_{\rm Edd} + b$.

† Spearman's rank correlation coefficient.

Dependence of Mg II/Fe II, Mg II, and Fe II on $L_{\rm bol}/L_{\rm Edd}$ is highlighted in Figure 4. Negative correlation against $L_{\rm bol}/L_{\rm Edd}$ is clearly seen for Mg II/Fe II and EW(Mg II). On the other hand, EW(Fe II) has a tentative, positive correlation with $L_{\rm bol}/L_{\rm Edd}$. We have performed linear regression analysis using the BCES(Y|X) method (Akritas & Bershady 1996), which takes into account measurement errors on both variables. The result is summarized in Table 1, where the calculated Spearman's correlation coefficients are also listed.

It is worth mentioning the preceding research by Dong et al. (2011). They analyzed 4,178 Seyfert 1 galaxies and quasars selected from SDSS DR4 for which redshifts are $z \leq 0.8$. They reported that the Fe II/Mg II flux ratio positively correlates with the Eddington ratio, which is consistent with our result. Note that they analyzed both UV and optical Fe II emission lines, therefore the redshift range of their sample is restricted. Compared with their analysis, we have used the later version of the SDSS data and concentrated on the UV Fe II emission line, which has increased the sample size by almost four times and widened the redshift range. One of the most interesting results of Dong et al. (2011) is that narrow Fe II emission in optical has a stronger correlation with the Eddington ratio than Mg II. Whether the narrow Fe II emission line exists in UV is unclear and investigating it is beyond the scope of this paper, but we may safely say that the slight correlation between the UV Fe II and the Eddington ratio seen in Figure 4 implies that contribution from the narrow Fe II emission in UV is small.

The Mg II/Fe II–$L_{\rm bol}/L_{\rm Edd}$ correlation is thus evident from observation, but the background physics behind it has not been well understood so far. In the following part of this paper, we investigate the origin of such emission-line correlations with the Eddington ratio.

4. PHOTOIONIZATION CALCULATIONS

Photoionization calculations have been carried out to investigate how Mg II and Fe II emission lines emitted from a BLR cloud depend on non-abundance parameters such as gas density, the ionization parameter, total H column density, spectral energy distribution (SED) of the illuminating source, and microturbulence. The values of

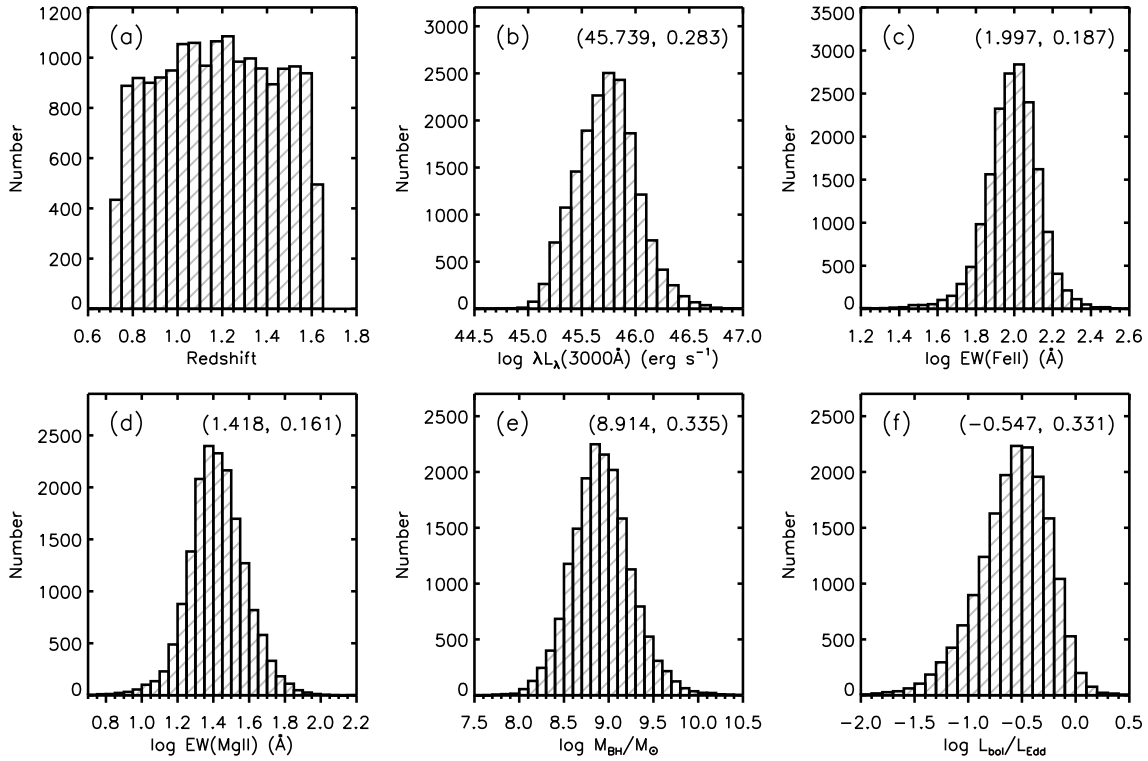

FIG. 1.— Histograms of the measured values for our sample of SDSS quasars: (a) redshift, (b) monochromatic luminosity at 3000Å, (c) EW(Fe II), (d) EW(Mg II), (e) BH mass, and (f) Eddington ratio. On each panel except for (a), both the median value and the standard deviation are given in the upper-right corner in parentheses (median, 1σ).

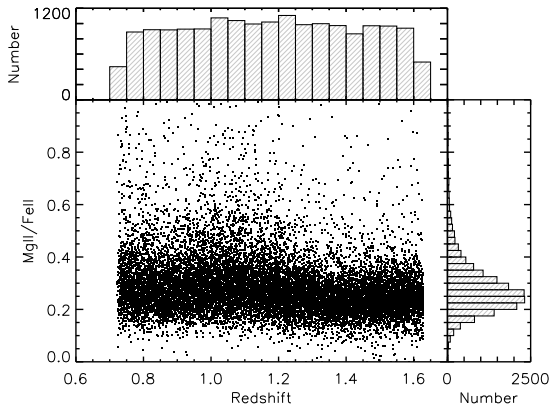

FIG. 2.— Mg II/Fe II flux ratio versus redshift for our sample of SDSS quasars. The histograms of flux ratio and redshift are shown in the right and upper panels, respectively.

these parameters are varied in their plausible respective ranges in calculations. In this section, we first explain the constraints on these parameters inferred from recent studies of BLR reverberation mapping. Then, we explain our choice of fiducial parameter values for a BLR cloud.

4.1. *Constraint on the property of a BLR cloud inferred from reverberation mapping studies*

Recent studies of BLR reverberation mapping (e.g., Peterson et al. 2004; Kaspi et al. 2005; Bentz et al. 2006, 2009, 2013) have revealed the so-called radius–luminosity relationship; the reverberation radius is larger for more luminous AGNs. From naive theoretical consideration, $R \propto L^{0.5}$ is naturally expected under the assumption that the central radiation field is the only source of heating and ionization. In fact, Bentz et al. (2013) measured Hβ lag times of 41 nearby AGNs from BLR reverberation mapping observations, and showed that the radius–luminosity relationship holds for AGNs over four orders of magnitude in luminosity.

Although there exist few studies of reverberation mapping for the Mg II emitting region, Metzroth et al. (2006) report that the Mg II reverberation radius is almost the same as Hβ for NGC 4151. Recently, Shen et al. (2016) report Mg II lag detection of 6 quasars at $0.3 < z < 0.8$, which also supports overlap between the regions in which Mg II and Hβ originate. Under the situation that no reliable lag detection at $z > 0.8$ is available, it is reasonable to assume that the Mg II emission line is created in the same region as Hβ even at $z > 0.8$. Thus, we assume that the radius–luminosity relationship for Mg II is the same as for Hβ given in Bentz et al. (2013), and is written as

$$\frac{R_{\rm MgII}}{10\ {\rm lt\text{-}days}} = (3.40 \pm 0.20) \left[\frac{\lambda L_\lambda (5100\text{Å})}{10^{44}\ {\rm erg\ s^{-1}}}\right]^{0.5}, \qquad (6)$$

where $R_{\rm MgII}$ is the Mg II reverberation radius. Note that we here adopt the power index of 0.5, as theoretically expected. The coefficient in equation (6) is determined by fitting a slope-fixed straight line to the data of Bentz et al. (2013).

This radius–luminosity relationship places an important constraint on the physical quantities of a BLR cloud. Let U be the ionization parameter defined as

$$U = \frac{\Phi({\rm H})}{n_{\rm H} c}, \qquad (7)$$

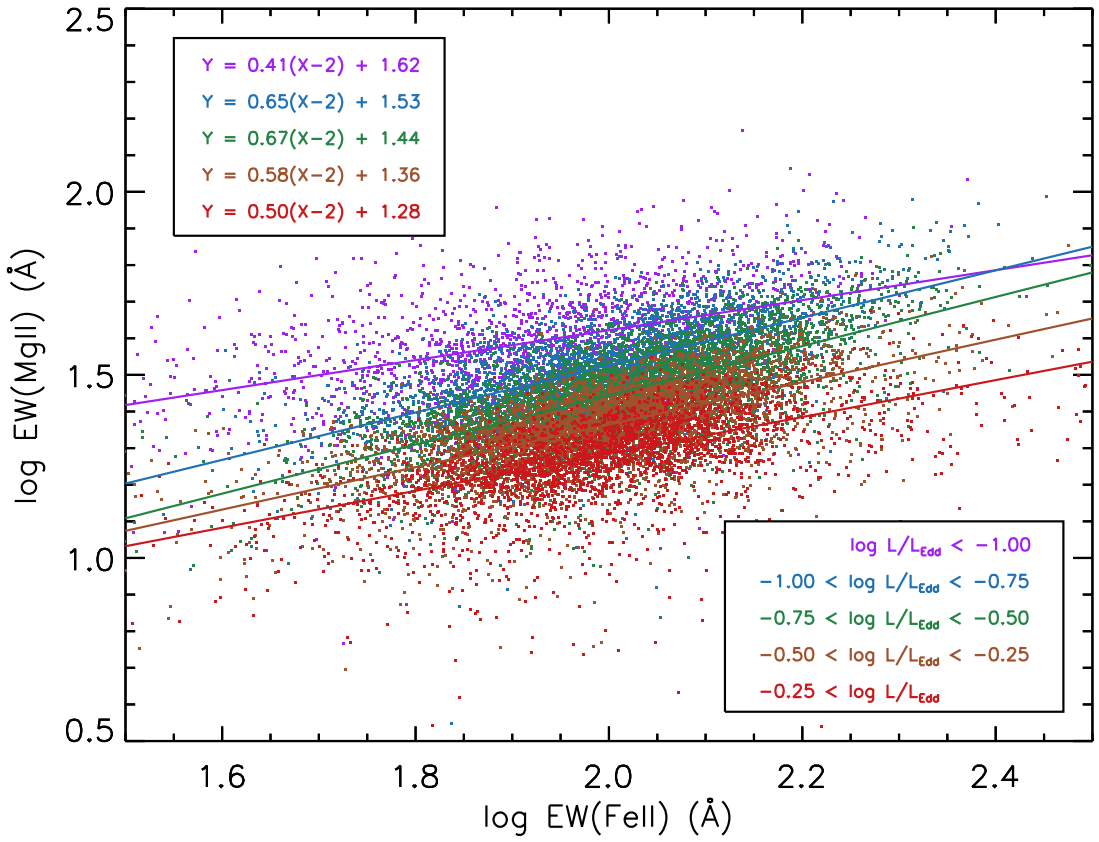
Y = 0.41(X−2) + 1.62
Y = 0.65(X−2) + 1.53
Y = 0.67(X−2) + 1.44
Y = 0.58(X−2) + 1.36
Y = 0.50(X−2) + 1.28
log L/L_Edd < −1.00
−1.00 < log L/L_Edd < −0.75
−0.75 < log L/L_Edd < −0.50
−0.50 < log L/L_Edd < −0.25
−0.25 < log L/L_Edd
log EW(MgII) (Å)
log EW(FeII) (Å)

FIG. 3.— EW(Mg II) versus EW(Fe II) diagram. The SDSS quasars from our sample in different ranges of the Eddington ratio are colored accordingly: $L_{\rm bol}/L_{\rm Edd} < 10^{-1.0}$ (purple), $10^{-1.0}$–$10^{-0.75}$ (blue), $10^{-0.75}$–$10^{-0.5}$ (green), $10^{-0.5}$–$10^{-0.25}$ (brown), and $> 10^{-0.25}$ (red). Linear regression analyses are performed for these sub-samples, and the results are given in the inset in the upper-left corner.

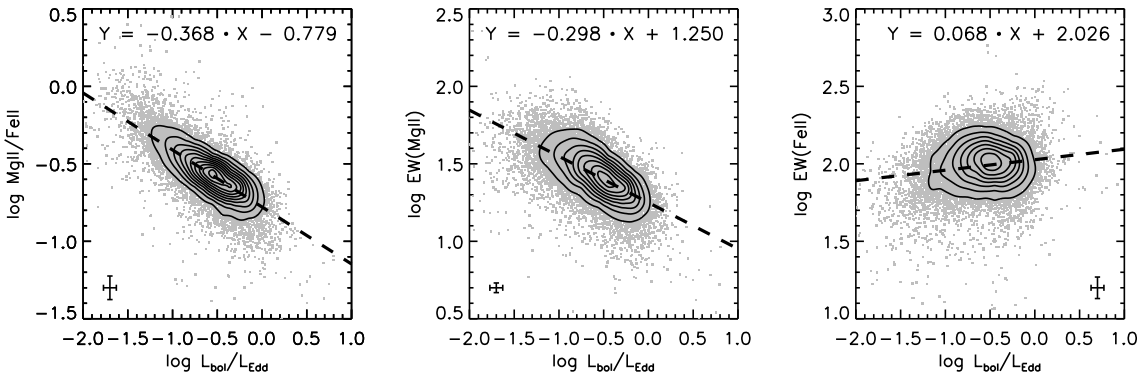

FIG. 4.— Dependence of emission-line strength on the Eddington ratio for our sample of SDSS quasars. (a) Mg II/Fe II, (b) EW(Mg II), (c) EW(Fe II). The contours indicate local data point densities with a grid size of $\Delta = 0.01$ dex. The dashed line indicates a linear regression line. The typical size of measurement errors are indicated at the corner of each panel.

where $n_{\rm H}$ is the hydrogen number density of the gas, c is the speed of light, and $\Phi({\rm H})$ is the incident hydrogen-ionizing photon flux. Furthermore, $\Phi({\rm H})$ can be reduced to

$$\Phi({\rm H}) = \int_{\nu_0}^{\infty} \frac{F_\nu}{h\nu} d\nu = \frac{1}{4\pi R^2} \int_{\nu_0}^{\infty} \frac{L_\nu}{h\nu} d\nu \equiv \frac{Q({\rm H})}{4\pi R^2}, \quad (8)$$

where ν_0 is the frequency corresponding to the ionization energy of H^0 (13.6 eV), F_ν is the flux density of the incident continuum at the illuminated face of a cloud, L_ν is the luminosity of the central source at frequency ν, and $Q({\rm H})$ is the number of hydrogen-ionizing photons emitted per second from the source. From equations (6)–(8), the product of $n_{\rm H}$ and U for the Mg II emitting region yields

$$n_{\rm H} U = (3.42 \pm 0.40) \times 10^{-2} \left(\frac{Q({\rm H})}{\lambda L_\lambda (5100{\rm \AA})} \right) \ {\rm cm}^{-3}, \quad (9)$$

where the term $Q({\rm H})/\lambda L_\lambda(5100{\rm \AA})$ depends only on the SED of the incident continuum.

Following the user manual of the CLOUDY code (last

described by Ferland et al. 2013), we have modeled the SED of an AGN as follows:

$$F_\nu = \nu^{\alpha_{\rm uv}} \exp(-h\nu/kT_{\rm BB}) \exp(-kT_{\rm IR}/h\nu) + a\nu^{\alpha_{\rm x}}, \quad (10)$$

where the first term on the right-hand side indicates the so-called *big blue bump* component, and the second term indicates the non-thermal X-ray component. The former is modeled as a power law with the index $\alpha_{\rm uv}$, which has exponential cutoffs at the energies of $kT_{\rm BB}$ and $kT_{\rm IR}$; the latter is modeled as a power law with the index $\alpha_{\rm x}$, which is truncated at energies less than 1.36 eV in order to prevent it from extending into the infrared part, and falls off as ν^{-2} at energies larger than 100 keV. The coefficient a, which determines a fraction between the two components, is uniquely determined if the well-used optical to X-ray spectral index $\alpha_{\rm ox}$[8] and the spectral indices $\alpha_{\rm uv}, \alpha_{\rm x}$ are once specified. Following Korista et al. (1997), we adopt $\alpha_{\rm ox} = -1.40$, $\alpha_{\rm uv} = -0.50$, $\alpha_{\rm x} = -1.0$, $T_{\rm BB} = 10^6$ K, and $kT_{\rm IR} = 0.136$ eV to reproduce the SED of a typical AGN. This results in $a = 3.5\times10^6$ and $Q({\rm H})/\lambda L_\lambda(5100{\rm \AA}) = 8.36\times10^{10}$ erg^{-1}. Substituting the latter value into equation (9), we obtain $n_{\rm H}U = (2.86 \pm 0.33) \times 10^9$ cm^{-3} or $n_{\rm H}U \sim 10^{9.5}$ cm^{-3}. To evaluate the dependence of SED diversity observed in quasars (e.g., Richards et al. 2006), we have varied the X-ray power-law index $\alpha_{\rm x}$ and the spectral index $\alpha_{\rm ox}$ in a wide range of $-2 \le \alpha_{\rm x} \le 0$ and $-2 \le \alpha_{\rm ox} \le -1$, respectively, from the above SED. The resultant value of $n_{\rm H}U$, however, changes only by 0.2 dex. It is thus appropriate to assume that all quasars in our sample follow $n_{\rm H}U \sim 10^{9.5}$ cm^{-3}. We note that this constraint is always taken into account in the following photoionization calculations of the Mg II and Fe II emission lines.

4.2. *Parameter setting*

We use the photoionization simulation code of Cloudy version 13.02, combined with the 371 level Fe^+ model that includes all energy levels up to 11.6 eV (Verner et al. 1999). The parameters for a BLR cloud required to run the code are the hydrogen gas density $n_{\rm H}$, the ionization parameter U, the SED of the illuminating source, the elemental abundance in the gas, and the column density that determines the outer edge of the cloud.

From the measured emission-line strengths and their ratios, the BLR gas density is estimated to be $n_{\rm H} = 10^{10}$–10^{12} cm^{-3} (e.g., Rees et al. 1989; Ferland et al. 1992; Baldwin et al. 1996). A fiducial value of the ionization parameter is estimated to be $U \sim 10^{-1}$ (e.g., Baskin et al. 2014), but Matsuoka et al. (2007) report that an O I emitting region in the BLR cloud, from which the Mg II and Fe II emission lines are also expected to originate, has a value of $U \sim 10^{-2.5}$. Combining these implications and the constraint $n_{\rm H}U = 10^{9.5}$ cm^{-3} inferred from the reverberation mapping studies, we adopt $n_{\rm H} = 10^{11}$ cm^{-3} and $U = 10^{-1.5}$ as the fiducial parameter values.

The SED of the illuminating source is set as in the previous section to reproduce the SED of a typical AGN, i.e., equation (10) and the following parameters are adopted: $\alpha_{\rm ox} = -1.40$, $\alpha_{\rm uv} = -0.50$, $\alpha_{\rm x} = -1.0$, $T_{\rm BB} = 10^6$ K, and $T_{\rm IR} = 0.136$ eV.

[8] $\alpha_{\rm ox} \equiv \log\left[f_\nu(2\ {\rm keV})/f_\nu(2500{\rm \AA})\right] / \log(403.3)$.

TABLE 2
Solar abundance

Element	$\log n$	Element	$\log n$	Element	$\log n$
H	0.00	Na	−5.76	Sc	−8.85
He	−1.07	Mg	−4.40	Ti	−7.05
Li	−10.95	Al	−5.55	V	−8.07
Be	−10.62	Si	−4.49	Cr	−6.36
B	−9.30	P	−6.59	Mn	−6.57
C	−3.57	S	−4.88	Fe	−4.50
N	−4.17	Cl	−6.50	Co	−7.01
O	−3.31	Ar	−5.60	Ni	−5.78
F	−7.44	K	−6.97	Cu	−7.81
Ne	−4.07	Ca	−5.66	Zn	−7.44

Note. — The values indicate the logarithmic number density relative to hydrogen.

Although there are only a few studies of observational constraints on the column density of the BLR cloud, many photoionization calculations assume that $N_{\rm H} = 10^{23}$ cm^{-2} (e.g., Baldwin et al. 1995, 2004; Korista et al. 1997; Matsuoka et al. 2008). Sameshima et al. (2011) proposed that the optical Fe II to UV Fe II flux ratio can be used as a column density indicator; they found its median value for 884 SDSS DR5 quasars to be $N_{\rm H} = 10^{22.8}$ cm^{-2}. Accordingly, we adopt $N_{\rm H} = 10^{23}$ cm^{-2} as the fiducial value.

For chemical composition, we assume the solar abundances of Asplund et al. (2009) as the fiducial, which are summarized in Table 2. Since Fe and Mg are refractory elements, their abundances would be largely affected by dust depletion. However, we conclude that ignoring the dust depletion in our simulations is reasonable for the following reason. Shields et al. (2010) proposed that the strength of optical Fe II emission lines in AGNs, which may originate from outside the BLR, may largely result from different degrees of the Fe depletion into dust grains. On the other hand, they also proposed that UV Fe II emission lines, which have been measured in this paper, originate in the BLR where dust grains evaporate, and are little affected by the dust depletion.

For metallicity, many studies suggest super-solar values for BLR clouds. For example, Hamann et al. (2002) estimated the BLR metallicity from emission lines to be 1–3 $Z_\odot$. Using similar methods, Nagao et al. (2006) reported that the typical metallicity of $2.0 < z < 4.5$ quasars is $\sim 5Z_\odot$. Since the redshift of our sample is relatively low ($0.72 < z < 1.63$), we here adopt $Z = 3Z_\odot$ as a fiducial value.

Most of the Fe II emission lines are emitted from collisionally excited levels. However, observed spectra show some Fe II emission lines from upper levels which are too high to have been collisionally excited by thermal electrons. This problem was overcome by adding microturbulence[9] to strengthen the photon pumping effect (e.g., Netzer & Wills 1983). From systematic photoionization calculations, Baldwin et al. (2004) showed that $v_{\rm turb} \ge 100$ km s^{-1} is needed to reproduce the observed Fe II spectral feature of a narrow-line Seyfert galaxy I Zw 1. In their recent study on Fe II emission in AGNs, Ferland et al. (2009) adopted $v_{\rm turb} = 100$ km s^{-1}.

[9] Magnetehydrodynamic waves are proposed as the origin of microturbulence for BLR clouds (Rees 1987; Bottorff & Ferland 2000), but it still remains an open research problem.

TABLE 3
PARAMETERS OF THE BASELINE MODEL FOR A BLR CLOUD

Parameter	Fiducial value
Hydrogen gas density $n_{\rm H}$	10^{11} cm^{-3}
Ionization parameter U	$10^{-1.5}$
Column density $N_{\rm H}$	10^{23} cm^{-2}
SED	Korista et al. (1997)
Elemental abundance pattern $x_{i,\odot}$	Solar (Table 2)
Metallicity Z	$3Z_\odot$
Microturbulence $v_{\rm turb}$	100 km s^{-1}

Therefore, we adopt $v_{\rm turb} = 100$ km s^{-1} as the fiducial value.

The fiducial parameter values of the baseline model are listed in Table 3. To investigate the parameter dependence, each parameter value is varied while other parameters are fixed in CLOUDY.

5. RESULTS

5.1. *Ionization structure*

The calculated ionization structure and electron temperature distribution in the BLR cloud for the baseline model are shown in Figure 5; the result for H and He is shown in the upper panel, while that for Mg and Fe is shown in the lower panel. Hydrogen is fully ionized from the cloud surface up to a depth of $D \sim 10^{11}$ cm, and is partially ionized in the deeper region. Because of the similarity in the ionization energies of Fe and Mg,[10] both Fe II and Mg II have generally been assumed to originate from the partially ionized zone (hereafter PIZ). However, the lower panel of Figure 5 indicates that an Mg^+ ion can survive in the fully ionized zone (hereafter FIZ) where almost all iron is ionized to Fe^{2+} or higher ion stages.

The difference between the ionization stages of Mg and Fe in the FIZ is explained as follows. Since thermal electrons at $T_{\rm e} \sim 10^4$ K do not have enough energy to collisionally ionize these ions, the ionization stage is substantially determined by a balance between photoionization and recombination. Figure 6 shows the photoionization cross sections of Fe^+ and Mg^+ as a function of photon energy, taken from Verner et al. (1996). While their threshold energies of ionization are similar ($\sim$ 15 eV), the photoionization cross section of Fe^+ is 1–2 orders of magnitude larger than that of Mg^+. Therefore, the ionization stage of Fe is higher than that of Mg at the same cloud depth in the FIZ.

5.2. *Line emissivity*

The calculated emissivities of the Mg II and Fe II lines for the baseline model are shown as a function of cloud depth in the upper panel of Figure 7. Note that the vertical axis is the line emissivity multiplied by the escape fraction β and the cloud depth D. As expected, the Fe II flux originates in the PIZ where the lines are mostly created. On the other hand, the emissivity of the Mg II line peaks in the FIZ, meaning that the Mg II flux originates in the FIZ, but *not* in the PIZ where Mg predominantly

[10] From Verner et al. (1996), the ionization energies of Fe in two different ion stages are 7.902 eV (Fe^0) and 16.19 eV (Fe^+), and those of Mg are 7.646 eV (Mg^0) and 15.04 eV (Mg^+).

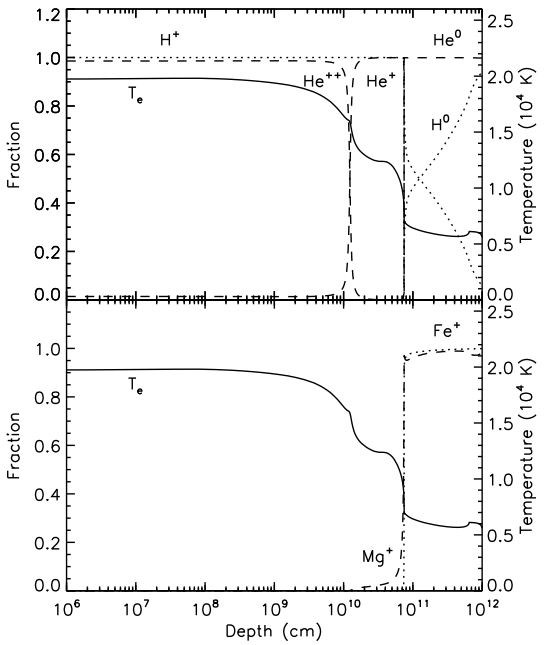

FIG. 5.— Ionization structure of a photoionized BLR cloud. *Top:* Fraction of H (dotted lines) and He (dashed lines) ions as a function of cloud depth from the illuminated face. The solid line indicates the electron temperature. *Bottom:* The same as the top panel, but for Fe^+ (dotted line) and Mg^+ (dashed line) ions.

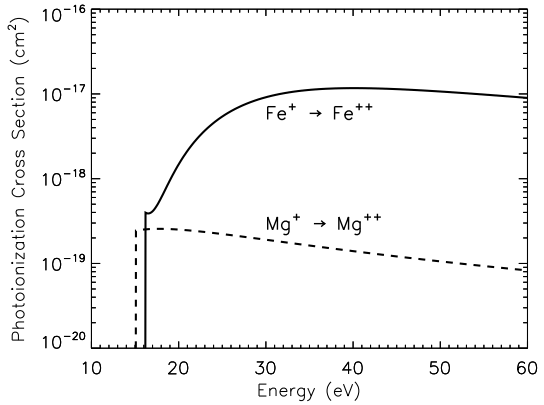

FIG. 6.— Photoionization cross section as a function of photon energy, taken from Verner et al. (1996). The solid and dashed lines indicate Fe^+ and Mg^+, respectively

exists in the form of Mg^+ ions. This is more clearly shown in the lower panel of Figure 7, where the vertical axis indicates the cumulative flux fraction.

The occurrence of the Mg II emissivity peak in the FIZ is explained as follows. First of all, since the Mg abundance is several orders smaller than H and He, the recombination of electrons with Mg^{2+} into the excited state of Mg^+ is superseded by collisional excitation of Mg^+ with electrons. Consider that an ion in the lower level 1 is excited to the upper level 2 by collision with electrons. Then, the excitation rate is written as $n_{\rm e} n_1 q_{12}$, where $n_{\rm e}$ is the electron density, n_1 is the ion density in level 1, and q_{12} is the rate coefficient for collisional excitation from level 1 to level 2 given by

$$q_{12} = \frac{8.629 \times 10^{-6}}{T_{\rm e}^{1/2}} \frac{\Upsilon(1,2)}{\omega_1} \exp(-\chi/kT_{\rm e}), \qquad (11)$$

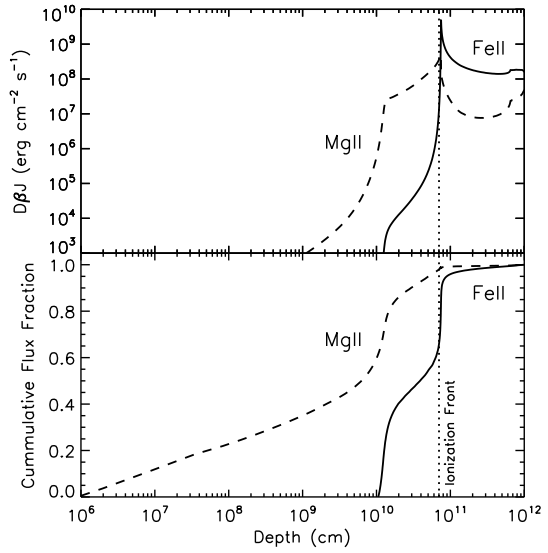

FIG. 7.— *Top:* Line emissivity as a function of cloud depth D for Fe II (solid line) and Mg II (dashed line). The vertical axis indicates $D\beta J$, where β is an escape probability of the photon, and J is an emissivity. Note that an emergent emission-line flux can be calculated by $\int D\beta J d(\ln D)$. The vertical dotted line indicates a boundary between the FIZ on the left and the PIZ on the right. *Bottom:* The same as the top panel, but the vertical axis indicates a cumulative flux fraction.

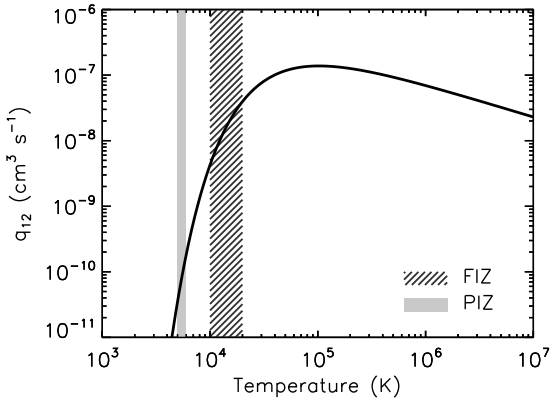

FIG. 8.— Mg II collisional excitation rate as a function of electron temperature. The line-filled and gray-filled areas indicate approximate ranges of electron temperature for the FIZ and the PIZ, respectively.

where $T_{\rm e}$ is the electron temperature, ω_1 is a statistical weight of level 1, χ is the excitation energy, and $\Upsilon(1,2)$ is a collision strength that varies slowly with $T_{\rm e}$ (Osterbrock & Ferland 2006). Figure 8 shows q_{12} as a function of $T_{\rm e}$ for the Mg II λ2798 emission line. It is evident that the rate coefficient at $T_{\rm e} \sim 10^4$ K in the FIZ is about two orders larger than at $T_{\rm e} \sim 5 \times 10^3$ K in the PIZ. In addition, the self absorption of line photons by abundant Mg^+ from the PIZ diminishes the emergent Mg II flux in that zone. As a result, the Mg II line emissivity peaks in the FIZ.

5.3. *Dependence on non-abundance parameters*

The calculated results for parameter dependence of emission lines are summarized in Figure 9. Each panel of this figure shows how the EWs of Mg II and Fe II, as well as the Mg II/Fe II flux ratio, change with the change of one particular parameter, while other parameters are fixed to their fiducial values of the baseline model. In the following, we explain the results for changing the hydrogen gas density $n_{\rm H}$, the column density $N_{\rm H}$, the SED of the incident continuum, and the microturbulence $v_{\rm turb}$.

The $n_{\rm H}$ dependence is shown in panel *a* of Figure 9. Note that $n_{\rm H}$ and U are varied simultaneously to keep their product constant ($n_{\rm H}U = 10^{9.5}$ cm^{-3}), according to the BLR reverberation constraint (see Section 4.1). As can clearly be seen, EW(Mg II) increases with increasing $n_{\rm H}$, while EW(Fe II) hardly changes with it. The physical reason for this is clear. In the FIZ, as $n_{\rm H}$ increases, $T_{\rm e}$ decreases and the fraction of Mg^+ ions increases (see Figure 10). This is due to enhanced recombination of $Mg^{2+} + e^- \rightarrow Mg^+$ for lower $T_{\rm e}$ because its rate is proportional to ${T_{\rm e}}^{-1/2}$. On the other hand, in the PIZ, $T_{\rm e}$ hardly changes, so that the fraction of Fe^+ and Mg^+ ions keeps almost unchanged. As a result, the strength of the Mg II emission line from the FIZ increases, while that of the Fe II emission line from the PIZ is kept almost constant.

The $N_{\rm H}$ dependence is shown in panel *b* of Figure 9. For $N_{\rm H} \lesssim 10^{22}$ cm^{-2}, both EW(Mg II) and EW(Fe II) change drastically. The Fe II emission line does not emerge from the PIZ, because the PIZ is not formed for such lower $N_{\rm H}$ and the gas is fully ionized throughout the cloud. Furthermore, below $N_{\rm H} \sim 10^{22}$ cm^{-2}, the Mg II emission line does not emerge from the FIZ, because the FIZ is not extended deeply enough to reach the Mg II line-forming region. The fact that most quasars show both Mg II and Fe II emission lines suggests that BLR clouds generally have $N_{\rm H} \gtrsim 10^{22}$ cm^{-2}. As $N_{\rm H}$ increases beyond 10^{22} cm^{-2}, the size of the PIZ increases. As a result, the strength of the Fe II emission line from the PIZ increases, while the strength of the Mg II emission line from the FIZ is unaffected. Note that Ferland et al. (2009) similarly argued for the $N_{\rm H}$ dependence of the emission line for Fe II, but not Mg II.

The results for varying the X-ray power-law index $\alpha_{\rm x}$ and the spectral index $\alpha_{\rm ox}$, both of which effectively determine the strength of the SED at $\gtrsim 1$ keV, are shown in panels *c* and *d* of Figure 9. Our photoionization calculations show that both EW(Mg II) and EW(Fe II) do not change very much with varying $\alpha_{\rm x}$ and $\alpha_{\rm ox}$. In particular, the changes of EW(Mg II) and Mg II/Fe II with the X-ray SED are too small to reproduce their observed ranges. Similar results are also reported by Shields et al. (2010). Because incident X-ray photons are widely assumed as the main heating source in the PIZ, it may seem strange that the Fe II emission depends little on the X-ray SED. In fact, our calculations indicate that harder SED gives rise to larger electron density and hence more cooling by Fe^+ ions especially at large cloud depth in the PIZ. However, the emissivities of those additionally created UV Fe II photons at large cloud depth are quite small due to their large optical depths there (see Figure 7). As a result, the emissivity of UV Fe II emission line as a whole is little affected by the X-ray SED of an illuminating source.

The dependence on the UV power-law index $\alpha_{\rm uv}$ is shown in panel *e* of Figure 9. As indicated in the figure, EW(Fe II) decreases with $\alpha_{\rm uv}$. This is mainly due to less incident photons having the energy less than 13.6 eV

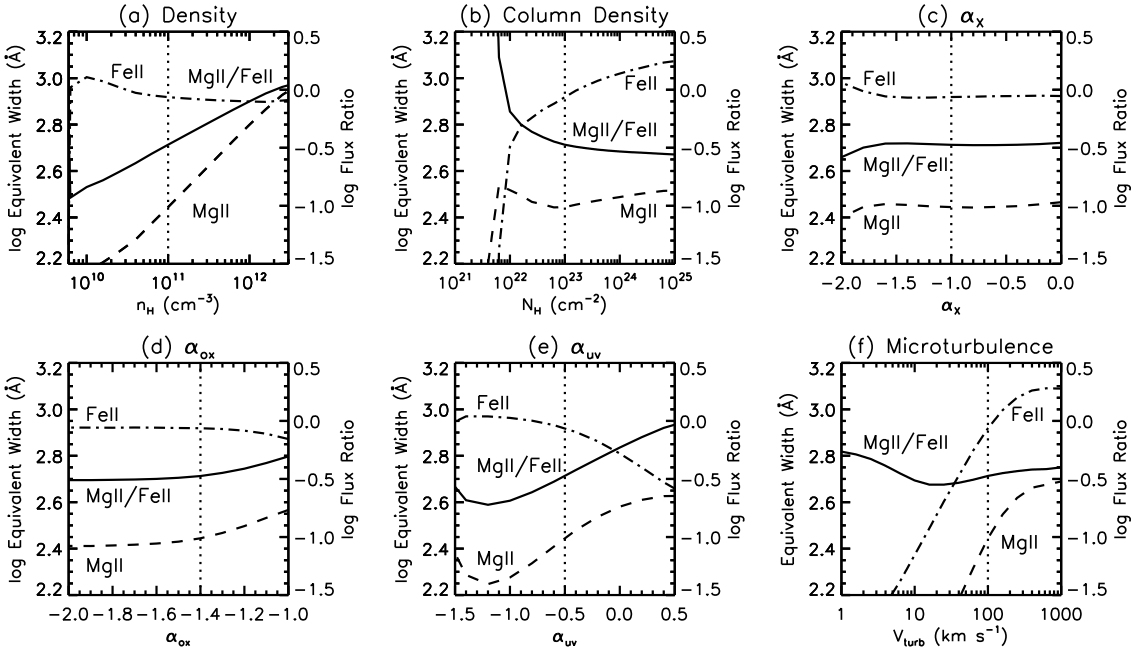

FIG. 9.— Dependence of the emission line on non-abundance parameters of the BLR cloud. Each panel shows the dependence on each parameter: (*a*) hydrogen gas density $n_{\rm H}$, (*b*) hydrogen column density $N_{\rm H}$, (*c*) X-ray power-law index $\alpha_{\rm x}$, (*d*) optical to X-ray spectral index $\alpha_{\rm ox}$, (*e*) UV power-law index $\alpha_{\rm uv}$ and (*f*) microturbulence $v_{\rm turb}$. The dash-dotted, dashed, and thick lines indicate EW(Fe II), EW(Mg II), and Mg II/Fe II, respectively. The vertical dotted line indicates the fiducial value of each parameter.

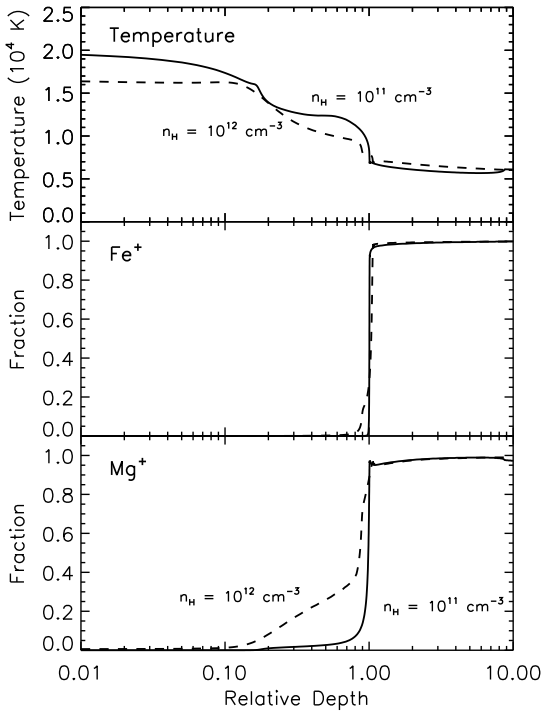

FIG. 10.— Change of electron temperature and ionization structure for different values of the BLR gas density. The horizontal axis indicates the relative depth of a cloud that is normalized at the ionization front. The vertical axes indicate electron temperature (*top panel*) and fractions of Fe^+ (*middle panel*) and Mg^+ (*bottom panel*). The solid and dashed lines shown on each panel are for $n_{\rm H} = 10^{11}$ cm^{-3} and 10^{12} cm^{-3}, respectively.

for larger $\alpha_{\rm uv}$. Those low-energy photons can penetrate the FIZ and photoexcite Fe^+ ions in the PIZ. Therefore, continuum pumping of Fe^+ ions and the resulting Fe II emission lines decrease when $\alpha_{\rm uv}$ increases. On the other hand, our photoionization calculations indicate that EW(Mg II) increases with $\alpha_{\rm uv}$. Moreover, we find that the line flux of Mg II hardly changes with $\alpha_{\rm uv}$; this result is understandable, because Mg II emission lines are mainly created at the FIZ which is transparent to those low energy photons with $E \lesssim 13.6$ eV. Thus, the increase of EW(Mg II) with $\alpha_{\rm uv}$ is mainly due to the decrease of continuum flux at 3000Å.

The $v_{\rm turb}$ dependence is shown in panel *f* of Figure 9. Larger $v_{\rm turb}$ gives rise to larger EW(Mg II) and EW(Fe II); this is because the local velocity difference in the moving medium decreases the self-absorption of the line photons, which causes them to escape more easily from the cloud. However, by calculating the Mg II/Fe II flux ratio, such $v_{\rm turb}$ dependence for each of the EWs is largely cancelled out. The resultant ratio hardly changes with $v_{\rm turb}$.

6. DISCUSSION

6.1. *Density dependence of the Mg II/Fe II flux ratio*

The assumption that the Mg II/Fe II flux ratio is a first-order proxy for the Mg/Fe abundance ratio would hold only if the Mg II and Fe II emission lines were found to originate from the same region owing to their similar ionization energies (e.g., Hamann & Ferland 1999). However, the result of our photoionization calculations shown in Figure 7 is highly suggestive of a difference in the emergent zone between the Mg II and Fe II emission lines; Mg II flux comes mostly from the FIZ, while Fe II flux comes from the PIZ. As can be seen from Figure 10, the ionization structure of a BLR cloud depends on the non-abundance parameter of $n_{\rm H}$, and more importantly, this $n_{\rm H}$ dependence for the FIZ is different

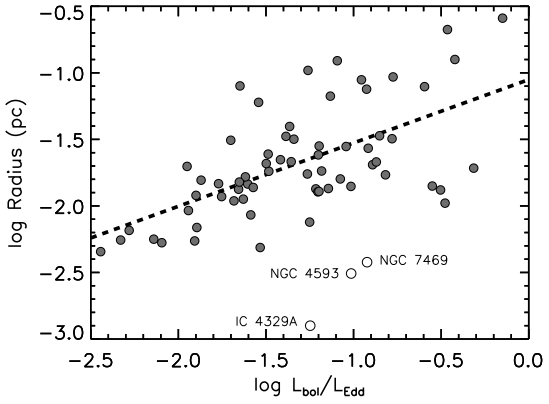

FIG. 11.— Distance to BLR clouds from the central source plotted against the Eddington ratio. The filled and open circles show the data taken from Bentz et al. (2009), and their black hole masses are retrieved from Peterson et al. (2004). The dashed line indicates the linear regression line. The open circles are removed from the regression analysis because of poor-quality lag measurement (IC 4329A and NGC 4593) and contamination from the nuclear starburst ring (NGC 7469).

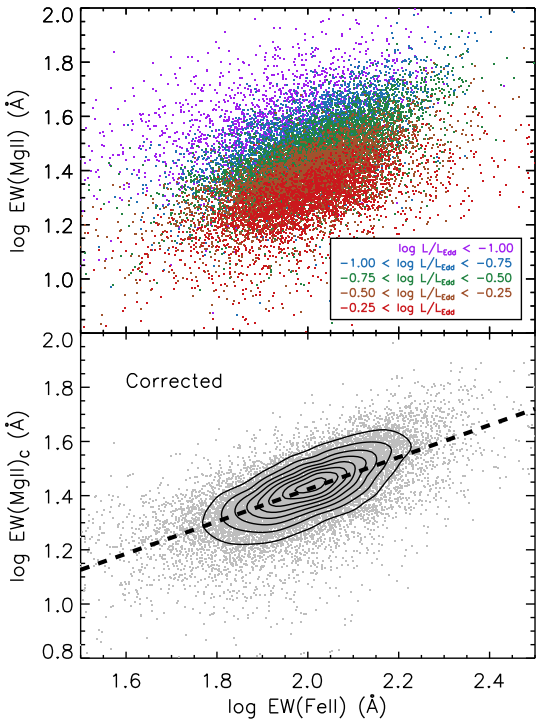
log EW(MgII) (Å)
log L/L$_{Edd}$ < −1.00
−1.00 < log L/L$_{Edd}$ < −0.75
−0.75 < log L/L$_{Edd}$ < −0.50
−0.50 < log L/L$_{Edd}$ < −0.25
−0.25 < log L/L$_{Edd}$
Corrected
log EW(MgII)$_c$ (Å)
log EW(FeII) (Å)

FIG. 12.— EW(Mg II) versus EW(Fe II) diagram. *Top:* The measured EW(Mg II)s for our sample of SDSS quasars are plotted against the measured EW(Fe II)s. Quasars are colored differently according to the different ranges of the Eddington ratio. *Bottom:* The EW(Mg II)s corrected for the density effect using equation (12) are plotted against the measured EW(Fe II)s as gray dots. The contours indicate local data point densities with a grid size of $\Delta = 0.01$ dex. The dashed line indicates a linear regression line.

from that for the PIZ. Thus, our result invalidates the assumption of Mg II/Fe II $\propto$ Mg/Fe, and indicates that the Mg II/Fe II flux ratio strongly depends on some non-abundance parameter other than the Mg/Fe abundance ratio. Our result therefore supports similar arguments previously given by other authors (e.g., Dong et al. 2011; De Rosa et al. 2011).

The Mg/Fe abundance ratio can then be derived from the Mg II/Fe II flux ratio *after* the effects of some non-abundance parameter, yet to be identified as a main driver of the existing correlations among observable quantities of quasars, have been properly corrected. Comparison of Figures 4 and 9 hints at a way of identifying such a parameter. Figure 4 indicates that Mg II emission-line flux correlates with $L_{\rm bol}/L_{\rm Edd}$, but Fe II emission-line flux does not. From the result of our photoionization calculations in Figure 9, those trends with $L_{\rm bol}/L_{\rm Edd}$ are fully reproduced solely by changing $n_{\rm H}$, when an anticorrelation exists between $n_{\rm H}$ and $L_{\rm bol}/L_{\rm Edd}$. On the other hand, those trends are not reproduced by changing either $N_{\rm H}$, the SED, or $v_{\rm turb}$. Therefore, it is reasonable to proceed with a hypothesis that the non-abundance parameter to be identified is mainly the BLR gas density that anticorrelates with the Eddington ratio, and the observed diversity of Mg II flux is partly attributed to object to object variation of the BLR gas density in quasars.

Our hypothesis of anticorrelation between $n_{\rm H}$ and $L_{\rm bol}/L_{\rm Edd}$ could be supported by the following discussion. For our sample of SDSS quasars, we obtain EW(Mg II) $\propto (L_{\rm bol}/L_{\rm Edd})^{-0.30}$ (Figure 4 and Table 1), and from our photoionization calculations, we find EW(Mg II) $\propto {n_{\rm H}}^{0.34}$ (Figure 9). These two relations are combined to give $n_{\rm H} \propto (L_{\rm bol}/L_{\rm Edd})^{-0.88}$. On the other hand, Rees et al. (1989) argued that the BLR gas density decreases with the increasing radial distance of the cloud away from the AGN center, i.e., $n_{\rm H} \propto R^{-s}$ $(1 < s < 2.5)$. Therefore, our hypothesis requires $R \propto (L_{\rm bol}/L_{\rm Edd})^{b}$, provided $b = 0.88/s$. We can check this requisite using the reverberation mapping data given in Bentz et al. (2009).[11] The result is shown in Figure 11, where a positive correlation is clearly seen. A linear regression analysis gives $b = 0.48$, leading to $s = 0.88/0.48 \sim 1.8$ within the limits of s in accordance with Rees et al. (1989). In this way, our hypothesis of anticorrelation between $n_{\rm H}$ and $L_{\rm bol}/L_{\rm Edd}$ is well confirmed by the data.

6.2. *Heavy-element abundance diagnostics with Mg II and Fe II emission lines*

Establishing a method of deriving heavy-element abundances of a BLR cloud is the most important problem in chemical evolution studies using quasars. For a long time, the Fe II/Mg II flux ratio has been used as a proxy for the Fe/Mg abundance ratio. However, as described in the previous section, we have reached the conclusion that the strength of the Mg II emission line strongly depends on the non-abundance parameter of the BLR gas density. Accordingly, the Mg II/Fe II flux ratio, unless corrected for the density effect, can never be used as a measure of the Mg/Fe abundance ratio. In this section, we describe a conversion of flux to abundance for quasars.

The first step is to correct EW(MgII) for the density effect, by scaling the observed EW(MgII) values of all

[11] The latest work on the radius–luminosity relationship by reverberation mapping measurement is given by Bentz et al. (2013), where six AGNs are newly added to those in Bentz et al. (2009). However, their black hole masses are not given, and it is not possible to estimate their Eddington ratios. Therefore, in this study, we use the data of Bentz et al. (2009) for which all black hole masses are available from Peterson et al. (2004).

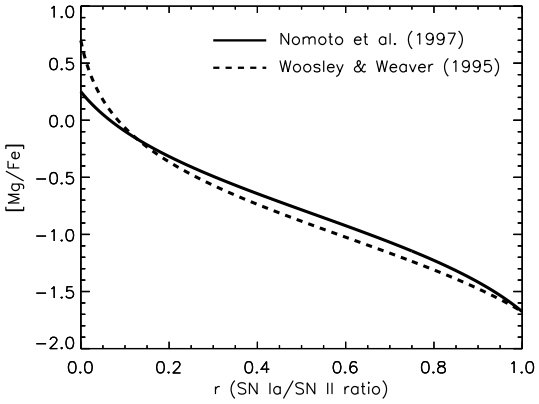

FIG. 13.— Logarithmic abundance ratio [Mg/Fe] as a function of r which represents the fraction of the SN Ia contribution in the abundance pattern. The solid and dashed lines indicate the results where the abundance pattern of SN II ejecta has been taken from Nomoto et al. (1997a) and Woosley & Weaver (1995), respectively.

quasars to those for the reference value of the Eddington ratio. The corrected EW(MgII) is given by

$$\mathrm{EW(MgII)_c} = \mathrm{EW(MgII)} \left(\frac{\langle L_{\rm bol}/L_{\rm Edd} \rangle}{L_{\rm bol}/L_{\rm Edd}} \right)^{-0.30}, \quad (12)$$

where $\langle L_{\rm bol}/L_{\rm Edd} \rangle = 10^{-0.55}$ is adopted as a median value of the measured Eddington ratios of the sample quasars (see Figure 1). Figure 12 shows the observed EW(Mg II) versus EW(Fe II) diagram in the upper panel, and the corrected EW(Mg II)$_{\rm c}$ versus EW(Fe II) diagram in the lower panel. Obviously, the scatter in the corrected EW(Mg II) data is, as a matter of course, decreased.

The second step is to bring about one-to-one correspondence between the (Mg/Fe, Fe/H) abundance pair and the (EW(Mg II)$_{\rm c}$, EW(Fe II)) pair, by running the CLOUDY simulation code with other non-abundance parameters fixed to the fiducial values given in Table 3. For realistic simulations with the heavy-element abundance pattern of stellar origin, we mix the yield patterns of SN Ia and SN II, following Tsujimoto et al. (1995). The ejecta masses of heavy elements for SN Ia are adopted from the W7 model in Nomoto et al. (1997b), and those for SN II are adopted from Nomoto et al. (1997a) and Woosley & Weaver (1995). Since the ejecta mass of each element for SN II depends on the mass of the progenitor star, we calculate the mean ejecta mass weighted by an initial mass function (IMF) of stars. Then the mean ejecta mass for the ith heavy element is given by

$$M_{i,\rm II} = \frac{\int_{m_{\rm min}}^{m_{\rm max}} M_{i,\rm II}(m) m^{-(1+\mu)} dm}{\int_{m_{\rm min}}^{m_{\rm max}} m^{-(1+\mu)} dm}, \quad (13)$$

where m is the mass of the progenitor star, $M_i(m)$ is the ith heavy-element mass produced in a main-sequence star of mass m, $m_{\rm min}$ and $m_{\rm max}$ are the lower and upper progenitor masses, and μ is the power index of the IMF. In this paper, we adopt $(m_{\rm min}, m_{\rm max}) = (10M_\odot, 50M_\odot)$ and $\mu = 1.35$, which represents the Salpeter IMF.

We introduce a parameter r for the mass fraction contributed by SN Ia per unit mass of all heavy elements. Then, the heavy-element abundance pattern is written as

$$x_i = r x_{i,\rm Ia} + (1-r) x_{i,\rm II}, \quad (14)$$

where $x_{i,\rm Ia} \equiv M_{i,\rm Ia} / \sum_{i=6}^{30} M_{i,\rm Ia}$ and $x_{i,\rm II} \equiv M_{i,\rm II} / \sum_{i=6}^{30} M_{i,\rm II}$. Note that since the elements given in Nomoto et al. (1997a) are from C to Zn, the index i in the above summation starts from 6 and ends at 30. The abundance ratio between Mg and Fe is equal to $x_{\rm Mg}/x_{\rm Fe}$, and in the following, for the sake of brevity, we denote Mg/Fe as the Mg/Fe abundance ratio in units of the solar ratio:

$$\mathrm{Mg/Fe} \equiv (x_{\rm Mg}/x_{\rm Fe}) \div (x_{\rm Mg,\odot}/x_{\rm Fe,\odot}), \quad (15)$$

where $x_{i,\odot} \equiv M_{i,\odot} / \sum_{i=6}^{30} M_{i,\odot}$ is the solar metal mass fraction calculated from Asplund et al. (2009). Accordingly, note that $\mathrm{Mg/Fe} \equiv 10^{\rm [Mg/Fe]}$. Figure 13 shows the logarithmic abundance ratio [Mg/Fe] as a function of r. We calculate the abundance pattern for the specific values of r corresponding to Mg/Fe=1/10, 1/8, 1/6, 1/4, 1/2, 1, 2, and 4, plus the case of $r = 0$ that stands for the pure SN II pattern. Tables 4 and 5 give the numerical form of the SN abundance pattern, using the SN II yields of Nomoto et al. (1997a) and Woosley & Weaver (1995), respectively.

In this study, for each of the x_i patterns having different Mg/Fe values as above, we run the CLOUDY code by scaling x_i so that the resultant grid of Fe/H is from 10^{-1} to 10^{+2} with a step of 0.2 dex to reflect the metallicity variation, with the shape of the x_i pattern unchanged. The results of the CLOUDY calculations are shown in Figure 14 for the case of Nomoto et al. (1997a) and Figure 15 for the case of Woosley & Weaver (1995), where the (Mg/Fe, [Fe/H]) grid is displayed on the corrected EW(Mg II)$_{\rm c}$ versus EW(Fe II) diagram (*top panel*). A point to be noted here is that the CLOUDY code is run with a covering factor of unity and the calculated EWs must be adjusted to the observation by scaling the covering factor of a BLR cloud. We find that the (Mg/Fe, [Fe/H]) grid with a covering factor of 0.13 nicely covers the measured EWs. This low value is fully consistent with previous independent reports (e.g., Peterson 1997, Netzer 2013), and is therefore used in Figures 14 and 15. A small fraction of measured EWs, however, lie outside the grid corresponding to the maximum Mg/Fe value expected from the pure SN II yields. This can be solved by placing more weight on massive progenitor and extending the grid towards larger Mg/Fe values. Additional calculations with increasing $m_{\rm min}$ beyond $10M_\odot$ in equation (13) are performed while fixing $m_{\rm max} = 50M_\odot$. The additional abundance patterns are tabulated in Tables 4 and 5, and the additional grids calculated with these abundance patterns are shown in gray in Figures 14 and 15.

The result that the measured EWs are covered by the (Mg/Fe, [Fe/H]) grid for reasonable respective ranges of Mg/Fe and [Fe/H] justifies our conversion of (EW(Mg II)$_{\rm c}$, EW(Fe II) to (Mg/Fe, [Fe/H]). As can be seen from Figures 14 and 15, the lines of constant Mg/Fe are slightly curved, non-orthogonal to those of constant [Fe/H], and inclined to the major axis of distribution of the measured EWs. Therefore, Mg/Fe, as well as [Fe/H], is a non-linear function of EW(Mg II)$_{\rm c}$ and EW(Fe II). For reference, Figures 14 and 15 show the de-

TABLE 4
ELEMENTAL ABUNDANCE PATTERN FOR DIFFERENT MIXTURES OF SN Ia AND SN II: NOMOTO ET AL. (1997A)

Mg/Fe† $(r, M_{\rm min}/M_\odot)$	1/10 (0.653, 10)	1/8 (0.585, 10)	1/6 (0.495, 10)	1/4 (0.372, 10)	1/2 (0.191, 10)	1 (0.066, 10)	1.781 (0, 10)	2 (0, 10.53)	4 (0, 14.07)	6 (0, 16.45)	8 (0, 19.20)	10 (0, 24.78)
C	−4.91	−4.88	−4.84	−4.76	−4.58	−4.36	−4.16	−4.05	−3.68	−3.56	−3.53	−3.50
N	−8.52	−8.41	−8.27	−8.08	−7.76	−7.45	−7.20	−6.14	−5.47	−5.52	−5.65	−5.89
O	−4.03	−3.94	−3.81	−3.64	−3.34	−3.04	−2.79	−2.74	−2.45	−2.27	−2.14	−2.00
F	−12.92	−12.87	−12.79	−12.67	−12.43	−12.16	−11.93	−11.93	−11.77	−11.65	−12.05	−12.02
Ne	−5.09	−4.98	−4.84	−4.65	−4.33	−4.03	−3.77	−3.73	−3.44	−3.26	−3.15	−3.06
Na	−6.70	−6.58	−6.44	−6.25	−5.93	−5.62	−5.36	−5.33	−5.05	−4.87	−4.76	−4.62
Mg	−5.40	−5.30	−5.18	−5.00	−4.70	−4.40	−4.15	−4.10	−3.80	−3.62	−3.50	−3.40
Al	−6.37	−6.27	−6.15	−5.97	−5.67	−5.37	−5.12	−5.06	−4.76	−4.58	−4.45	−4.32
Si	−4.81	−4.79	−4.76	−4.69	−4.55	−4.35	−4.16	−4.13	−3.91	−3.76	−3.66	−3.52
P	−7.26	−7.20	−7.12	−7.00	−6.76	−6.49	−6.26	−6.21	−5.92	−5.76	−5.64	−5.48
S	−5.16	−5.15	−5.13	−5.10	−5.02	−4.89	−4.74	−4.69	−4.43	−4.29	−4.19	−4.04
Cl	−7.87	−7.85	−7.83	−7.77	−7.65	−7.47	−7.29	−7.25	−7.01	−6.85	−6.74	−6.57
Ar	−5.94	−5.93	−5.92	−5.88	−5.80	−5.67	−5.52	−5.46	−5.19	−5.05	−4.94	−4.78
K	−8.19	−8.17	−8.14	−8.09	−7.96	−7.78	−7.60	−7.55	−7.29	−7.13	−7.01	−6.83
Ca	−6.10	−6.09	−6.08	−6.04	−5.96	−5.84	−5.69	−5.64	−5.38	−5.25	−5.15	−5.00
Sc	−10.80	−10.78	−10.74	−10.68	−10.53	−10.33	−10.13	−10.08	−9.80	−9.63	−9.51	−9.32
Ti	−7.85	−7.83	−7.81	−7.76	−7.64	−7.47	−7.29	−7.29	−7.21	−7.14	−7.09	−7.09
V	−8.61	−8.61	−8.61	−8.60	−8.59	−8.55	−8.51	−8.48	−8.30	−8.21	−8.16	−8.05
Cr	−6.53	−6.52	−6.52	−6.51	−6.49	−6.44	−6.38	−6.36	−6.20	−6.10	−6.05	−5.96
Mn	−6.46	−6.47	−6.47	−6.49	−6.54	−6.66	−6.95	−6.92	−6.75	−6.66	−6.63	−6.53
Fe	−4.50	−4.50	−4.50	−4.50	−4.50	−4.50	−4.50	−4.50	−4.50	−4.50	−4.50	−4.50
Co	−7.39	−7.40	−7.40	−7.41	−7.43	−7.49	−7.59	−7.60	−7.65	−7.66	−7.66	−7.94
Ni	−5.26	−5.26	−5.27	−5.28	−5.33	−5.44	−5.72	−5.72	−5.72	−5.76	−5.78	−5.86
Cu	−9.97	−9.96	−9.93	−9.88	−9.75	−9.58	−9.40	−9.40	−9.41	−9.36	−9.31	−9.68
Zn	−8.84	−8.82	−8.79	−8.73	−8.59	−8.41	−8.21	−8.23	−8.29	−8.32	−8.30	−8.73

NOTE. — The values are the logarithmic number density of each element relative to hydrogen. All heavy elements are scaled so that the resultant [Fe/H] equals 0.

† $\mathrm{Mg/Fe} \equiv 10^{[\mathrm{Mg/Fe}]}$.

TABLE 5
ELEMENTAL ABUNDANCE PATTERN FOR DIFFERENT MIXTURES OF SN Ia AND SN II: WOOSLEY & WEAVER (1995)

Mg/Fe† $(r, M_{\rm min}/M_\odot)$	1/10 (0.582, 10)	1/8 (0.513, 10)	1/6 (0.427, 10)	1/4 (0.318, 10)	1/2 (0.174, 10)	1 (0.084, 10)	2 (0.032, 10)	4 (0.005, 10)	5.280 (0, 10)	6 (0, 13.73)	8 (0, 20.57)	10 (0, 24.49)
C	−4.57	−4.49	−4.38	−4.22	−3.94	−3.65	−3.34	−3.04	−2.96	−2.91	−2.89	−2.85
N	−5.27	−5.15	−5.01	−4.81	−4.49	−4.18	−3.87	−3.56	−3.47	−3.47	−3.41	−3.34
O	−3.96	−3.86	−3.73	−3.55	−3.25	−2.95	−2.64	−2.33	−2.25	−2.15	−2.03	−1.99
F	−8.46	−8.34	−8.20	−8.00	−7.68	−7.37	−7.06	−6.75	−6.66	−6.60	−6.49	−6.39
Ne	−4.95	−4.84	−4.70	−4.51	−4.19	−3.88	−3.57	−3.26	−3.18	−3.10	−3.00	−2.89
Na	−6.60	−6.48	−6.34	−6.14	−5.82	−5.52	−5.20	−4.90	−4.81	−4.75	−4.67	−4.54
Mg	−5.40	−5.30	−5.18	−5.00	−4.70	−4.40	−4.09	−3.79	−3.70	−3.62	−3.50	−3.40
Al	−6.32	−6.22	−6.10	−5.92	−5.61	−5.31	−5.00	−4.70	−4.61	−4.52	−4.36	−4.26
Si	−4.75	−4.71	−4.65	−4.56	−4.36	−4.13	−3.85	−3.57	−3.48	−3.43	−3.43	−3.60
P	−7.07	−6.99	−6.88	−6.72	−6.44	−6.15	−5.85	−5.55	−5.46	−5.38	−5.28	−5.33
S	−5.07	−5.04	−4.99	−4.91	−4.73	−4.50	−4.23	−3.95	−3.87	−3.83	−3.89	−4.21
Cl	−7.51	−7.43	−7.32	−7.17	−6.89	−6.60	−6.29	−5.99	−5.91	−5.86	−5.83	−6.14
Ar	−5.85	−5.82	−5.77	−5.68	−5.49	−5.26	−4.99	−4.71	−4.62	−4.60	−4.66	−5.00
K	−7.79	−7.71	−7.60	−7.44	−7.15	−6.86	−6.56	−6.26	−6.17	−6.19	−6.19	−6.55
Ca	−6.03	−6.01	−5.97	−5.89	−5.72	−5.51	−5.25	−4.98	−4.89	−4.88	−4.98	−5.26
Sc	−10.16	−10.06	−9.93	−9.75	−9.45	−9.15	−8.84	−8.54	−8.45	−8.41	−8.33	−8.61
Ti	−7.85	−7.83	−7.81	−7.76	−7.64	−7.47	−7.25	−7.00	−6.92	−6.92	−6.91	−6.95
V	−8.60	−8.59	−8.58	−8.56	−8.51	−8.42	−8.28	−8.09	−8.02	−8.02	−7.98	−7.96
Cr	−6.53	−6.53	−6.53	−6.52	−6.51	−6.48	−6.42	−6.33	−6.30	−6.30	−6.30	−6.30
Mn	−6.45	−6.45	−6.45	−6.45	−6.46	−6.47	−6.50	−6.55	−6.58	−6.59	−6.56	−6.51
Fe	−4.50	−4.50	−4.50	−4.50	−4.50	−4.50	−4.50	−4.50	−4.50	−4.50	−4.50	−4.50
Co	−7.36	−7.35	−7.34	−7.32	−7.26	−7.15	−6.99	−6.79	−6.72	−6.66	−6.58	−6.53
Ni	−5.23	−5.23	−5.23	−5.22	−5.20	−5.15	−5.08	−4.95	−4.91	−5.18	−5.23	−5.36
Cu	−8.70	−8.59	−8.45	−8.26	−7.94	−7.63	−7.32	−7.01	−6.93	−6.83	−6.69	−6.65
Zn	−8.07	−7.96	−7.83	−7.65	−7.34	−7.03	−6.72	−6.42	−6.33	−6.23	−6.06	−6.00

NOTE. — The values are the logarithmic number density of each element relative to hydrogen. All heavy elements are scaled so that the resultant [Fe/H] equals 0.

† $\mathrm{Mg/Fe} \equiv 10^{[\mathrm{Mg/Fe}]}$.

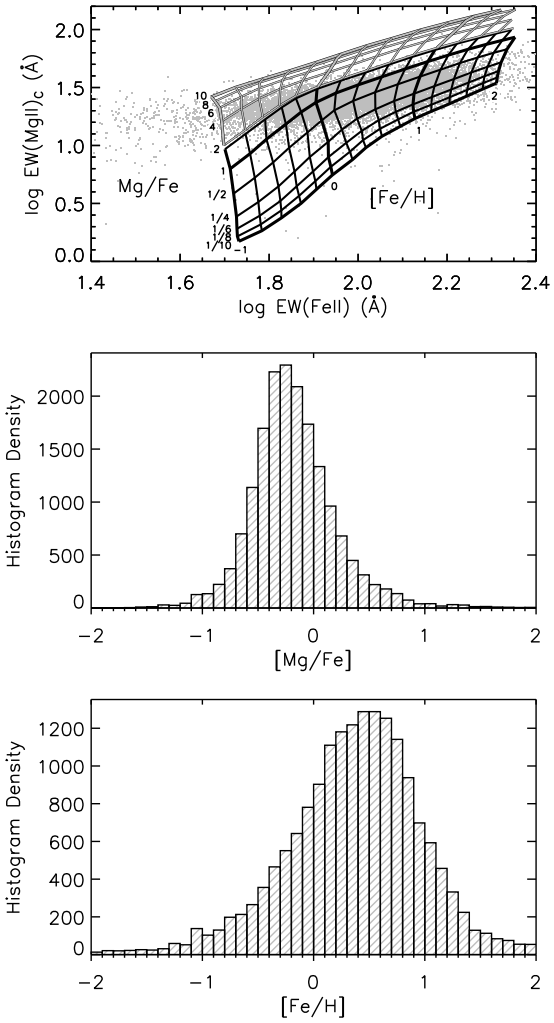

FIG. 14.— Measurements of Fe and Mg abundances of our sample quasars from Fe II and Mg II emission lines, based on our photoionization calculations using the SN heavy-element abundance pattern (Table 4) from the SN II yields of Nomoto et al. (1997a). *Top:* The calculated grid of the (Mg/Fe, [Fe/H]) abundance pair overlaid on the EW(Mg II)$_c$ versus EW(Fe II) diagram. The gray grid is based on additional calculations placing more weight on massive progenitor (see text). The measured EW(Mg II)$_c$ of our SDSS quasars, which have been corrected for the density effect, are shown by gray dots. *Middle:* Histogram of the logarithmic abundance ratio [Mg/Fe] with a bin size of 0.1 dex. *Bottom:* Histogram of metallicity [Fe/H] with a bin size of 0.1 dex.

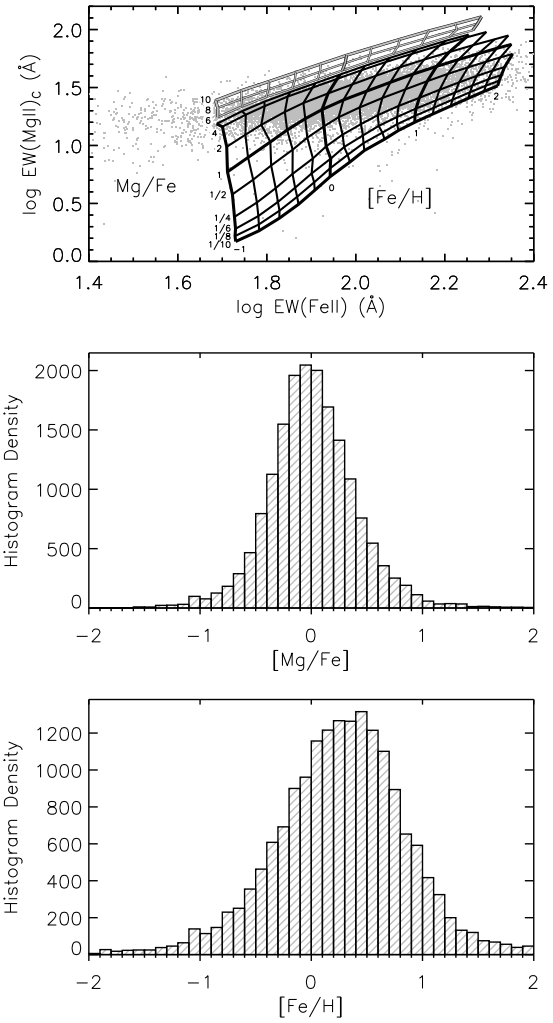

FIG. 15.— Measurements of Fe and Mg abundances of our sample quasars from Fe II and Mg II emission lines. The same as Figure 14, but with the SN heavy-element abundance pattern (Table 5) from the SN II yields of Woosley & Weaver (1995).

rived distributions of [Mg/Fe] (*middle panel*) and [Fe/H] (*bottom panel*) for our sample of SDSS quasars. Typical uncertainties of the measured [Mg/Fe] and [Fe/H] are estimated to be 0.27 dex and 0.32 dex, respectively, from the error propagation of the measurement errors on EW(Mg II) and EW(Fe II). With no alternative methods reported previously, this conversion is the first attempt to reliably extract the abundance information from the emission lines of metals.

6.3. *Evolution of [Mg/Fe] and [Fe/H]*

The goal of this study is to constrain the star formation history in the Universe from the chemical evolution of quasar host galaxies. In contrast with previous studies, in which the Mg II/Fe II flux ratio is used as the Mg/Fe abundance ratio, our proposed method allows measurement of the Mg/Fe abundance ratio, enabling direct comparison with theoretical chemical evolution models. Figure 16 (*top panel*) shows the result of [Mg/Fe] as a function of redshift for our SDSS quasars plotted in Figure 14. The mean values of the derived [Mg/Fe] abundance ratios in each redshift bin ($\Delta z = 0.15$) are indicated by filled boxes. The error bars indicate $\sqrt{\sigma^2 - \sigma^2_{\rm mes}}$, where σ is the standard deviation of the derived [Mg/Fe] abundance ratios in each redshift bin and $\sigma_{\rm mes}$ is the measurement error of [Mg/Fe] estimated in the previous subsection. Therefore, they represent systematic errors of the covering factor and the parameters listed in Table 3. Given that a lot of parameters are fixed to the fiducial values, the derived error bars are so small that support the validity of our assumptions. The SN II yields of Nomoto et al. (1997a) are used in the figure, but it should be noted that even if those of Woosley & Weaver (1995) are used, the result remains almost the same except for a small offset in [Mg/Fe]. Figure 16 (*bottom panel*) shows the result of [Fe/H] as a function of redshift, in the same way as [Mg/Fe].

In the figure, shown by curves are the chemical evolu-

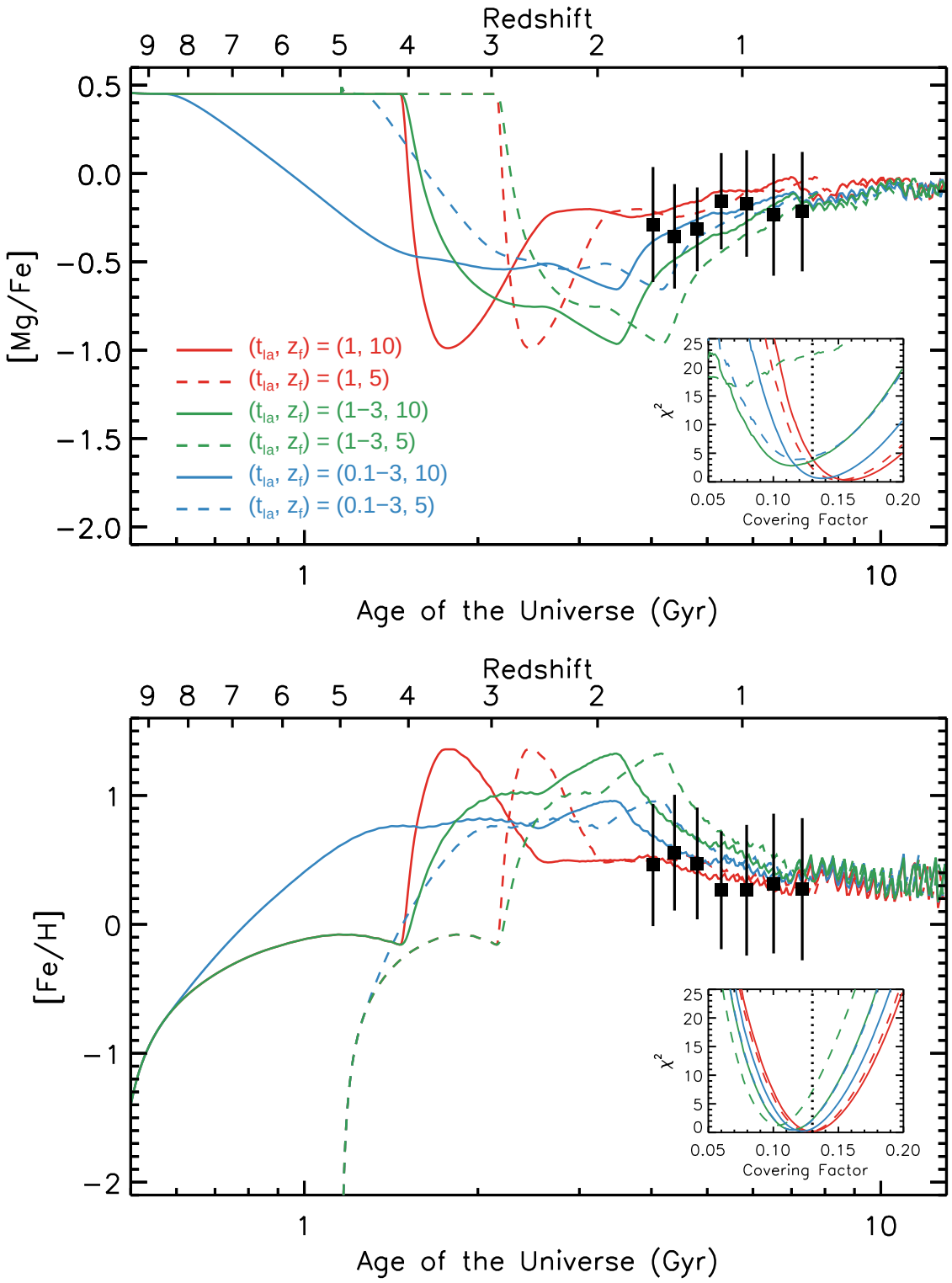

FIG. 16.— Comparison of various chemical evolution models with derived [Mg/Fe] abundance ratios (*top panel*) and [Fe/H] abundance ratios (*bottom panel*) as a function of redshift for our sample of SDSS quasars. The mean values and $\sqrt{\sigma^2 - \sigma^2_{\rm mes}}$ of the derived [Mg/Fe] and [Fe/H] abundance ratios in each redshift bin ($\Delta z = 0.15$) are indicated by filled boxes and error bars, respectively. The overplotted curves are the chemical evolution models of quasar host galaxies for several prescriptions of the SN Ia lifetime and the star formation epoch. Note that the jagged pattern at $z \lesssim 1$ in each model is artificial due to the finite time steps in the model calculations. In the inset, a chi-squared value is plotted as a function of the covering factor for each of the chemical evolution models, and the adopted covering factor of 0.13 in this study is indicated by a vertical dotted line. Note that the SN II yields of Nomoto et al. (1997a) are used to derive [Mg/Fe] and [Fe/H].

tion models of quasar host galaxies with an initial burst of star formation and the time-invariant Salpeter IMF (for details, see Yoshii et al. 1998). Three types of the SN Ia lifetime are considered: a single lifetime model with $t_{\rm Ia} = 1$ Gyr, a box-shaped $t_{\rm Ia}$ distribution model with 1–3 Gyr (Yoshii et al. 1996), and a power-law $t_{\rm Ia}$ distribution model with $g(t_{\rm Ia}) \propto t_{\rm Ia}^{-0.1}$ for 0.1–3 Gyr (Totani et al. 2008). For each of these three types, two values of the initial star formation redshift are considered: $z_f = 5$ and 10. In general, the [Mg/Fe] ratio is initially maintained at a level as high as +0.5 dex, reflecting the [Mg/Fe] ratio of the SN II ejecta averaged with the time-invariant Salpeter IMF, and then the onset of SNe Ia with the enhanced Fe supply causes a sudden fall and rise of theoretical curves of [Mg/Fe] and [Fe/H], respectively. After SNe Ia have ended their lives, a significant number of metal-poor intermediate-mass stars, which were formed initially from the metal-deficient gas with high [Mg/Fe] of pure SN II origin, start to lose their envelope mass in the the surrounding gas. This can be seen as upward turn of [Mg/Fe] and downward turn of [Fe/H] at $z \sim 2-3$. Since the effect of mass loss becomes small with z, the theoretical curves of [Mg/Fe] and [Fe/H] eventually reach their respective constant levels at $z < 1$.

The most important thing to note from Figure 16 is that our measurements of [Mg/Fe] and [Fe/H] at redshift below $z < 2$ lie along the theoretical curves. This means that unless the effect of later mass loss is taken into account in the models, the theoretical curves will continue to fall in [Mg/Fe] and rise in [Fe/H] with decreasing z and become unable to agree with our measurements at $z < 2$. Therefore, the result in Figure 16 strongly suggests that the mass loss of intermediate-mass stars did occur in quasars.

Another point to note is that the predictions at $z > 2$ largely differ from model to model, although they tend to converge at $z < 2$. From the inset diagram of Figure 16 (*top panel*), we may safely say that the three models adopting $(t_{\rm Ia}, z_f)$=(1–3, 5), (1–3, 10) and (0.1–3, 5) are rejected because χ^2 values of those models are clearly larger than the other models. However, the convergence of models at low redshift prevents us from distinguishing which is the best model in the remaining three models from our sample of SDSS quasars. For this reason, high-redshift data are vitally important to overcome the indistinguishability among the models at $z < 2$. In the forthcoming paper, we will give a more complete discussion on the chemical evolution of the Universe by also analyzing the available Fe II/Mg II data at $z > 2$.

Comparing our result with chemical evolution studies using other kind of objects, such as damped Lyman-α (DLA) absorbers, is also of interest. As can be seen from Figure 6 in Rafelski et al. (2012), the metallicity of DLA is sub-solar and decreases with increasing redshift, both of which are quite different from our result. However, it is not surprising given that BLR clouds and DLA absorbers are totally different objects; the former likely reside in elliptical galaxies, while the latter are likely associated with star-forming galaxies. The difference between their host galaxies and star formation histories may account for the different behavior of chemical evolution. On the other hand, several studies indicate that sub-DLAs appear to be metal rich. For example, Figure 11

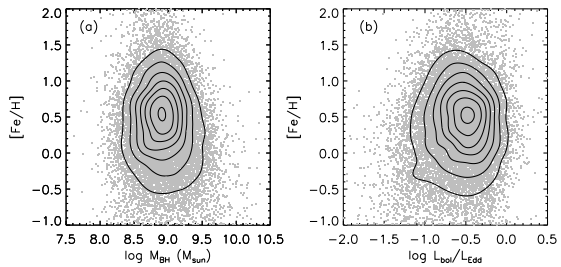

FIG. 17.— Dependence of metallicity on (a) black hole mass and (b) the Eddington ratio. The contours indicate local data point densities with a grid size of $\Delta = 0.01$ dex.

in Som et al. (2015) indicates that the sub-DLA metallicity is super-solar at $z < 1$, which is consistent with our result. It is interesting to note that Chartas et al. (2013) observed 21 quasars, which are known to contain sub-DLAs in their spectra, with the *Chandra* X-ray observatory. They found possible X-ray emission within $\sim 1''$ of the background quasar in six cases. Both of these results suggest that sub-DLAs may be associated with AGNs. Further investigation on this aspect would give insights into galaxy evolution.

It remains, however, a challenge for future research to investigate the systematic errors of our new abundance diagnostics. In particular, the assumptions worthy of mention for the fiducial quantities of a typical BLR cloud include the gas density of 10^{11} cm^{-3} and the covering factor of 0.13. The fiducial gas density determines an anchor point of the grid shown in Figures 14 and 15 in a vertical direction, resulting in a systematic error for [Mg/Fe]. On the other hand, the fiducial covering factor determines an anchor point of the grid in a diagonal direction, resulting in systematic errors for both [Mg/Fe] and [Fe/H]. It should be noted, however, that the covering factor changes the estimated [Mg/Fe] and [Fe/H] in the opposite direction, and is uniquely determined by comparing the chemical evolution models at low redshift. Improving the accuracy of these estimates would require analysis of other emission lines together with Fe II and Mg II, which would make it possible to more fully investigate the chemical evolution of the Universe with quasar emission lines.

6.4. *Black hole mass and metallicity*

There has been a growing interest in a relationship between black hole mass and other quasar properties. We have checked whether the metallicity, measured by our method, depends on black hole mass or not. The result is shown in Figure 17. Evidently, apparent correlation is not confirmed. We also plot the metallicity against the Eddington ratio, but the result is similar. Several authors report the existence of correlations between these quantities and the N V/C IV flux ratio, which is frequently used as an indicator of BLR metallicity (e.g., Shemmer et al. 2004, Matsuoka et al. 2011). Investigating the difference between their result and ours is beyond the scope of this paper, but it may be due to the density dependence of N V and/or C IV, or different origination between highly ionized lines such as N V and C IV and less highly ionized lines such as Fe II.

7. SUMMARY AND CONCLUSION

For the purpose of inventing abundance diagnostics for a BLR cloud, we selected 17,432 quasars from the SDSS DR7 data and analyzed their Mg II and Fe II emission lines. In addition to their emission-line strengths, we measured their black hole masses and Eddington ratios. As a result, an anticorrelation was found to exist between the Mg II/Fe II flux ratio and the Eddington ratio; this is largely due to the anticorrelation between the Mg II line strength and the Eddington ratio.

How and where Mg II and Fe II emission lines are created in a BLR cloud was investigated by photoionization calculations using CLOUDY. Taking into account the results of recent reverberation mapping studies, our calculations show that Mg II and Fe II are created in different regions of a BLR cloud. This indicates that the Mg II/Fe II flux ratio depends not only on the Mg/Fe abundance ratio but also on other non-abundance parameters. Therefore, the Mg II/Fe II flux ratio corrected for the non-abundance parameter has to be used for the abundance diagnostics.

In order to identify the main cause that accounts for the observed trends of the Mg II and Fe II emission-line strengths, extensive calculations were carried out by varying each of the non-abundance parameters in CLOUDY, such as BLR gas density, column density, SED of the incident continuum, and microturbulence. It was found that the observed trends can be reproduced solely by changing the BLR gas density. We have thus concluded that the trend of Mg II/Fe II with the Eddington ratio for our sample of SDSS quasars requires the existence of anticorrelation between the BLR gas density and the Eddington ratio.

Accordingly, Mg II/Fe II corrected for the density effect should reflect the abundance ratio more directly. To confirm this expectation, the corrected EW(Mg II)$_c$ versus EW(Fe II) diagram is compared with calculations from CLOUDY, where the Mg/Fe abundance ratio and the metallicity [Fe/H] are varied with other non-abundance parameters fixed to their fiducial values for the baseline model of a BLR cloud. It is found that the data in the diagram are distributed within the calculated grid of Mg/Fe and [Fe/H] for their reasonable respective ranges. This indicates that our abundance diagnostics works well for a BLR cloud, and more reliable estimates of the gas density and covering factor for a BLR cloud further enhance the accuracy of the resultant estimates of abundance parameter values.

For our sample of SDSS quasars at $z < 2$, we have derived [Mg/Fe] ~ -0.2 and [Fe/H] $\sim +0.5$ on the average, which more or less agrees with chemical evolution models in which the effect of mass loss from initially formed metal-poor intermediate-mass stars is explicitly taken into account. These models, although tending to converge at $z < 2$, predict the diversity in [Mg/Fe] at $z > 2$. Therefore, high-redshift data are essential for distinguishing the best model from many plausible ones at $z < 2$. We will discuss this in the forthcoming paper.

Finally, we have compared the derived [Fe/H] with black hole mass and the Eddington ratio. Contrary to the earlier studies using the N V/C IV flux ratio as an indicator of BLR metallicity, no apparent correlation between them is confirmed. Although investing the origin of the difference is beyond the scope of this paper, it may be due to the density dependence of N V and/or C IV, or different origination between highly ionized lines such as N V and C IV and less highly ionized lines such as Fe II.

We acknowledge the anonymous referee for constructive comments that helped to improve the quality of our manuscript. We thank Takuji Tsujimoto and Toshihiro Kawaguchi for helpful discussions. This work was supported by Grant-in-Aid for JSPS Fellows Grant Number 12J10755, and JSPS KAKENHI Grant Number 22253002. Funding for the SDSS and SDSS-II has been provided by the Alfred P. Sloan Foundation, the Participating Institutions, the National Science Foundation, the U.S. Department of Energy, the National Aeronautics and Space Administration, the Japanese Monbukagakusho, the Max Planck Society, and the Higher Education Funding Council for England. The SDSS Web Site is http://www.sdss.org/. The SDSS is managed by the Astrophysical Research Consortium for the Participating Institutions. The Participating Institutions are the American Museum of Natural History, Astrophysical Institute Potsdam, University of Basel, University of Cambridge, Case Western Reserve University, University of Chicago, Drexel University, Fermilab, the Institute for Advanced Study, the Japan Participation Group, Johns Hopkins University, the Joint Institute for Nuclear Astrophysics, the Kavli Institute for Particle Astrophysics and Cosmology, the Korean Scientist Group, the Chinese Academy of Sciences (LAMOST), Los Alamos National Laboratory, the Max-Planck-Institute for Astronomy (MPIA), the Max-Planck-Institute for Astrophysics (MPA), New Mexico State University, Ohio State University, University of Pittsburgh, University of Portsmouth, Princeton University, the United States Naval Observatory, and the University of Washington.

REFERENCES

Akritas, M. G., & Bershady, M. A. 1996, ApJ, 470, 706
Asplund, M., Grevesse, N., Sauval, A. J., & Scott, P. 2009, ARA&A, 47, 481
Baldwin, J., Ferland, G., Korista, K., & Verner, D. 1995, ApJ, 455, L119
Baldwin, J. A., Ferland, G. J., Korista, K. T., Hamann, F., & LaCluyzé, A. 2004, ApJ, 615, 610
Baldwin, J. A., Ferland, G. J., Korista, K. T., et al. 1996, ApJ, 461, 664
Barth, A. J., Martini, P., Nelson, C. H., & Ho, L. C. 2003, ApJ, 594, L95
Barth, A. J., Pancoast, A., Bennert, V. N., et al. 2013, ApJ, 769, 128
Baskin, A., Laor, A., & Stern, J. 2014, MNRAS, 438, 604
Bentz, M. C., Peterson, B. M., Netzer, H., Pogge, R. W., & Vestergaard, M. 2009, ApJ, 697, 160
Bentz, M. C., Peterson, B. M., Pogge, R. W., Vestergaard, M., & Onken, C. A. 2006, ApJ, 644, 133
Bentz, M. C., Denney, K. D., Grier, C. J., et al. 2013, ApJ, 767, 149
Bottorff, M. C., & Ferland, G. J. 2000, MNRAS, 316, 103
Chartas, G., Kulkarni, V. P., & Asper, A. 2013, ApJ, 775, 119
Chelouche, D., Rafter, S. E., Cotlier, G. I., Kaspi, S., & Barth, A. J. 2014, ApJ, 783, L34
Collin-Souffrin, S., Joly, M., Dumont, S., & Heidmann, N. 1980, A&A, 83, 190
Collin-Souffrin, S., Joly, M., Heidmann, N., & Dumont, S. 1979, A&A, 72, 293

Davies, R. I., Müller Sánchez, F., Genzel, R., et al. 2007, ApJ, 671, 1388
De Rosa, G., Decarli, R., Walter, F., et al. 2011, ApJ, 739, 56
De Rosa, G., Venemans, B. P., Decarli, R., et al. 2014, ApJ, 790, 145
Dietrich, M., Appenzeller, I., Vestergaard, M., & Wagner, S. J. 2002, ApJ, 564, 581
Dietrich, M., Hamann, F., Appenzeller, I., & Vestergaard, M. 2003, ApJ, 596, 817
Dong, X.-B., Wang, J.-G., Ho, L. C., et al. 2011, ApJ, 736, 86
Ferland, G. J., Hu, C., Wang, J.-M., et al. 2009, ApJ, 707, L82
Ferland, G. J., Peterson, B. M., Horne, K., Welsh, W. F., & Nahar, S. N. 1992, ApJ, 387, 95
Ferland, G. J., Porter, R. L., van Hoof, P. A. M., et al. 2013, Rev. Mexicana Astron. Astrofis., 49, 137
Freudling, W., Corbin, M. R., & Korista, K. T. 2003, ApJ, 587, L67
Grandi, S. A. 1981, ApJ, 251, 451
—. 1982, ApJ, 255, 25
Greggio, L., & Renzini, A. 1983, A&A, 118, 217
Hamann, F., & Ferland, G. 1993, ApJ, 418, 11
—. 1999, ARA&A, 37, 487
Hamann, F., Korista, K. T., Ferland, G. J., Warner, C., & Baldwin, J. 2002, ApJ, 564, 592
Iwamuro, F., Kimura, M., Eto, S., et al. 2004, ApJ, 614, 69
Iwamuro, F., Motohara, K., Maihara, T., et al. 2002, ApJ, 565, 63
Jiang, L., Fan, X., Vestergaard, M., et al. 2007, AJ, 134, 1150
Joly, M. 1981, A&A, 102, 321
Kaspi, S., Maoz, D., Netzer, H., et al. 2005, ApJ, 629, 61
Kawara, K., Murayama, T., Taniguchi, Y., & Arimoto, N. 1996, ApJ, 470, L85
Korista, K., Baldwin, J., Ferland, G., & Verner, D. 1997, ApJS, 108, 401
Kurk, J. D., Walter, F., Fan, X., et al. 2007, ApJ, 669, 32
Kwan, J., & Krolik, J. H. 1981, ApJ, 250, 478
Maiolino, R., Juarez, Y., Mujica, R., Nagar, N. M., & Oliva, E. 2003, ApJ, 596, L155
Maoz, D., Mannucci, F., & Brandt, T. D. 2012, MNRAS, 426, 3282
Markwardt, C. B. 2009, in Astronomical Society of the Pacific Conference Series, Vol. 411, Astronomical Data Analysis Software and Systems XVIII, ed. D. A. Bohlender, D. Durand, & P. Dowler, 251
Marziani, P., Sulentic, J. W., Zamanov, R., et al. 2003, ApJS, 145, 199
Matsuoka, K., Nagao, T., Marconi, A., Maiolino, R., & Taniguchi, Y. 2011, A&A, 527, A100
Matsuoka, Y., Kawara, K., & Oyabu, S. 2008, ApJ, 673, 62
Matsuoka, Y., Oyabu, S., Tsuzuki, Y., & Kawara, K. 2007, ApJ, 663, 781
Matteucci, F., & Greggio, L. 1986, A&A, 154, 279
Metzroth, K. G., Onken, C. A., & Peterson, B. M. 2006, ApJ, 647, 901
Mortlock, D. J., Warren, S. J., Venemans, B. P., et al. 2011, Nature, 474, 616
Nagao, T., Marconi, A., & Maiolino, R. 2006, A&A, 447, 157
Netzer, H. 2013, The Physics and Evolution of Active Galactic Nuclei (UK: Cambridge University Press)
Netzer, H., & Wills, B. J. 1983, ApJ, 275, 445
Nomoto, K., Hashimoto, M., Tsujimoto, T., et al. 1997a, Nuclear Physics A, 616, 79
Nomoto, K., Iwamoto, K., Nakasato, N., et al. 1997b, Nuclear Physics A, 621, 467
Osterbrock, D. E. 1977, ApJ, 215, 733
Osterbrock, D. E., & Ferland, G. J. 2006, Astrophysics of gaseous nebulae and active galactic nuclei (CA: University Science Books)
Peterson, B. M. 1997, An Introduction to Active Galactic Nuclei (New York Cambridge University Press)
Peterson, B. M., Ferrarese, L., Gilbert, K. M., et al. 2004, ApJ, 613, 682
Phillips, M. M. 1978a, ApJS, 38, 187
—. 1978b, ApJ, 226, 736
Rafelski, M., Wolfe, A. M., Prochaska, J. X., Neeleman, M., & Mendez, A. J. 2012, ApJ, 755, 89
Rees, M. J. 1987, MNRAS, 228, 47P
Rees, M. J., Netzer, H., & Ferland, G. J. 1989, ApJ, 347, 640
Richards, G. T., Lacy, M., Storrie-Lombardi, L. J., et al. 2006, ApJS, 166, 470
Sameshima, H., Kawara, K., Matsuoka, Y., et al. 2011, MNRAS, 410, 1018
Sameshima, H., Maza, J., Matsuoka, Y., et al. 2009, MNRAS, 395, 1087
Schneider, D. P., Richards, G. T., & Hall, P. B. 2010, AJ, 139, 2360
Shemmer, O., Netzer, H., Maiolino, R., et al. 2004, ApJ, 614, 547
Shen, Y., Richards, G. T., Strauss, M. A., et al. 2011, ApJS, 194, 45
Shen, Y., Horne, K., Grier, C. J., et al. 2016, ApJ, 818, 30
Shields, G. A., Ludwig, R. R., & Salviander, S. 2010, ApJ, 721, 1835
Som, D., Kulkarni, V. P., Meiring, J., et al. 2015, ApJ, 806, 25
Thompson, K. L., Hill, G. J., & Elston, R. 1999, ApJ, 515, 487
Totani, T., Morokuma, T., Oda, T., Doi, M., & Yasuda, N. 2008, PASJ, 60, 1327
Tsujimoto, T., Nomoto, K., Yoshii, Y., et al. 1995, MNRAS, 277, 945
Tsuzuki, Y., Kawara, K., Yoshii, Y., et al. 2006, ApJ, 650, 57
Verner, D. A., Ferland, G. J., Korista, K. T., & Yakovlev, D. G. 1996, ApJ, 465, 487
Verner, E., Bruhweiler, F., Verner, D., Johansson, S., & Gull, T. 2003, ApJ, 592, L59
Verner, E. M., Verner, D. A., Korista, K. T., et al. 1999, ApJS, 120, 101
Vestergaard, M., & Osmer, P. S. 2009, ApJ, 699, 800
Vestergaard, M., & Wilkes, B. J. 2001, ApJS, 134, 1
Wills, B. J., Netzer, H., & Wills, D. 1985, ApJ, 288, 94
Woosley, S. E., & Weaver, T. A. 1995, ApJS, 101, 181
York, D. G., Adelman, J., Anderson, Jr., J. E., et al. 2000, AJ, 120, 1579
Yoshii, Y., Tsujimoto, T., & Kawara, K. 1998, ApJ, 507, L113
Yoshii, Y., Tsujimoto, T., & Nomoto, K. 1996, ApJ, 462, 266